A Numerical Investigation of the Effects of Laser heating on Resonance Measurements of Nanocantilevers

by

Padmini Kutturu
B. Tech., JNTU, 2015

A Thesis Submitted in Partial Fulfillment
of the Requirements for the Degree of

MASTER OF APPLIED SCIENCE

in the Department of Mechanical Engineering

Supervisory Committee

A Numerical Investigation of the Effects of Laser heating on Resonance Measurements of Nanocantilevers

by

Padmini Kutturu
B.Tech, JNTU, 2015

Supervisory Committee

Dr. Rustom Bhiladvala, Supervisor
(Department of Mechanical Engineering)

Dr. Keivan Ahmadi, Committee member
(Department of Mechanical Engineering)

Abstract

Supervisory Committee
Dr. Rustom Bhiladvala, Supervisor
(Department of Mechanical Engineering)
Dr. Keivan Ahmadi, Committee member
(Department of Mechanical Engineering)

Nanomechanical resonators (NR) are cantilevers or doubly clamped nanowires (NW) which vibrate at their resonance frequency. These nanowires with picogram-level mass and frequencies of the order of MHz can resolve added mass in the attogram (10^{-18} g) range, enabling detection of a few molecules of cancer biomarkers based on the shift in resonance frequency. Such biomarker detection can help in the early stage detection of cancer and also aid in monitoring the treatment procedure in a more advanced stage.

Optical transduction is one of the methods to measure the resonance frequency of the cantilever. However, there is a dependence of measured resonance frequency on the polarization of light and the laser power coupled as thermal energy into the cantilever during the measurement. This thesis presents a numerical model of the nanocantilever and shows the variation in resonance frequency and amplitude due to varied amounts of energy absorption by the NW from the laser during resonance measurements.

This thesis answers questions on the effects of laser heating by calculating the temperature distribution in the NW, which changes the Young's modulus and stiffness, causing a resonance downshift. It also shows the variation of resonance amplitude, affecting signal strength in measurements, by considering the effects of structural damping.

In this work, a numerical model of the nanowire was analyzed to determine the temperature rise of the NW due to laser heating. The maximum temperature was calculated to be about 500 K with 1 mW of laser power absorbed in Silicon NWs and it is shown that the nanowire tip would reach its melting point for about 2.6 mW of laser power absorbed by it.

The resonance shift due to attained temperature of the NW was calculated. The frequency is predicted to decrease by 24 kHz for a 11.6 MHz resonator, when 2mW of laser power is absorbed. However, the frequency shift is mode-dependent and is larger for higher modes.

The variation in vibration amplitude around the resonance peaks is calculated based on the effects of structural damping. This can be used to decide on the suspension height of the NW above the substrate, before fabrication. This calculation also provides a method to study the variation in material damping due to temperature.

Finally, a semi-analytical method for calculating the frequency of a cantilever beam with varying Young's modulus is derived to examine the validity of the results calculated above. An effective Young's modulus value for the laser heated NW is given, which serves as a correction factor for the resonance shift. The derivation is then extended to calculate the resonance shift with an addition of a mass to the beam of varying Young's modulus.

Table of Contents

Supervisory Committee ii
Abstract iii
Table of Contents v
List of Tables viii
List of Figures ix
List of Abbreviations and symbols xi
Abbreviations xi
Symbols xi
Acknowledgments xiv
Dedication xv
Chapter 1: Introduction 1
1.1 Overview 1
1.2 Research Contributions 2
1.3 Thesis Structure 3
Chapter 2: Background and Literature Review 4
2.1 Overview 4
2.2 Role of NRs in biological sensing 4
2.3 Fabrication of nanomechanical resonators 4
2.3.1 Field-directed assembly of Nanoresonators (NR) 5
2.3.2 Other applications of Nanoresonators: 6
2.4 Nanoresonators (NR) for mass sensing 6
2.4.1 Actuation and detection techniques 7
2.4.1.1 Optical transduction method for resonance measurement 8
2.4.2 Resonance shift due to laser heating 9
2.5 Finite difference Methods (FDM) 11
Chapter 3: Numerical Model for Temperature Analysis of a Laser Heated Nanowire 13
3.1 Computational analysis for determining the temperature profile of nanowire . 13
3.1.1 Theoretical modelling of heat transport in SiNWs 13
3.1.2 Governing equations for Heat Transfer inside the Nanowire 14
3.1.3 Discretization of governing equations and boundary conditions: 17
3.1.4 Thomas Algorithm 19
3.2 Simulation Results and Discussion 19
3.2.1 Linear profile of the NW with constant conductivity in the case of convective losses 20
3.2.2 Variation in thermal conductivity of Si with temperature 22
3.2.3 Non-linear temperature profile with variable thermal conductivity for cases of convection and radiation 23
3.2.4 Maximum power that could be absorbed by the NW 24
3.2.5 Other thermal considerations at nanoscale 25
3.3 Conclusions and Recommendations 25
Chapter 4: Resonance Shift due to Laser Heating 26
4.1 Undamped multi degrees of freedom (MDOF) system: 26
4.1.1 Boundary conditions of nanocantilever: 28
4.1.2 Eigenvalues (ω_r^2) and Eigenvectors (ψ_r) of cantilever beam: 29

4.1.3 Modal Mass (m_r) and Modal Stiffness (k_r): 29
4.1.4 Mass-normalised mode shape for mode *r* ($\emptyset \boldsymbol{r}$): 30
4.2 Damping: 30
4.2.1 Internal damping: 31
4.2.2 Thermoelastic damping 31
4.2.3 Gas friction damping 31
4.3 Measurement of damping: 31
4.4 Calculation of damping matrix 32
4.5 Frequency response function (FRF) analysis 34
4.6 Verification of values for amplitude 34
4.7 Simulation results and discussion 35
4.7.1 Variation in Young's modulus of the nanowire due to its temperature distribution 35
4.7.2 Comparison of numerically calculated resonance with constant Young's modulus and a distributed Young's modulus 36
4.7.3 Calculation of resonance shift caused due to laser power 38
4.7.4 FRF for a constant Young's modulus, *E*, having a constant loss factor, η: 39
4.7.5 FRF for a distributed Young's modulus, *E*, and distributed loss factor, η: 40
4.7.6 Comparison of FRF for a distributed Young's modulus, *E*, with both constant and a distributed loss factor, η 42
4.7.7 Comparison of FRF of a stiffer nanowire with a softer nanowire: 42
Chapter 5: Euler-Bernoulli Derivation for a beam of varying Young's Modulus and a mass added at the tip 45
5.1 Derivation of general form of theoretical resonance frequency 45
5.2 Derivation of theoretical resonance frequency with varying stiffness 47
5.2.1 Boundary conditions of the nanocantilever 48
5.3 Calculation of resonance with an attached mass 50
5.3.1 Boundary conditions of the nanocantilever with an attached mass 50
5.4 Simulation results and discussion 52
5.4.1 Comparison of non-dimensional natural frequencies for a beam of uniform Young's modulus 52
5.4.2 Relative frequency shift for varying fractions of laser power due to distributed Young's modulus, *E* 53
5.4.3 Effective stiffness of the laser heated beam 54
5.4.4 Resonance shift due to attached mass at tip of the cantilever 57
5.4.5 Resonance shift due to mass attached at different locations of the cantilever 58
5.4.6 Comparison of frequency shift between Euler-Bernoulli, Semi-analytical, and the modal analysis models 59
5.5 Conclusion: 61
Chapter 6: Conclusions and Future work 63
Bibliography 66
Appendix A: 1. MATLAB code for temperature profile of NW considering conduction and/or convection 73
Appendix B: Analytical equation used to validate the convection process 77
Appendix C: MATLAB code for temperature profile of NW considering Radiation 78

Appendix D: MATLAB code for frequency response functions 82
Appendix E: MATLAB code for Semi-analytical method to calculate frequency of a beam with varying *E* and an attached mass 85
Appendix G: MATLAB code for analytical equation to calculate frequency of a beam with uniform *E* 88

List of Tables

Table 1: Comparing the non-dimensional natural frequencies, ω_{ND}, of Semi-analytical simulation results against Modal analysis, Euler-Bernoulli and Fundamental frequency Equation for a beam of uniform stiffness 52
Table 2: Effective Young's modulus *E* value for varying fractions of laser power 54
Table 3: Calculated frequencies (Hz) of NW with assumed modulus distributions $E_1(x)$, $E_2(x)$ and $E_3(x)$ as described in the text..... 56
Table 4: Resonance frequency of a beam with a mass of 3E-18 Kg attached at the tip of the cantilever..... 60

List of Figures

Figure 2.1 (a) Array of nanoresonators on the substrate fabricated by Field-directed method (b) Closer picture of one of the resonators on the substrate [16] 5
Figure 2.2 Resonance downshift due to attached mass 7
Figure 2.3 Optical measurement setup [30] displaying a frequency signal on spectrum analyser when laser is focused on the NW 9
Figure 2.4 schematic of optical measurement setup 10
Figure 2.5 Downshift of resonance frequency with increase in laser power [30] with A-21 and E-76 in the sub plot showing different Rhodium resonators on the same substrate .. 11
Figure 3.1 Silicon Nanowire description 14
Figure 3.2 Energy Balance in NW 15
Figure 3.3 Laser focused on tip of the NW showing BC's 18
Figure 3.4 Linear temperature profile of SiNW with convective losses 20
Figure 3.5 Varying the values of mL to make the profile non-linear by: (a) Increasing the h/k ratio (b) Increasing the surface area by reducing radius of the NW (c) Enhancing the aspect ratio by increasing length of the nanowire 21
Figure 3.6 Variation of Thermal conductivity with temperature 22
Figure 3.7 Temperature profile with: (a) convective losses at 2mW of power absorption (b) radiative losses at 2mW of power absorption by Si NW 23
Figure 3.8 Tip temperatures vs absorbed laser power by SiNW with radiative/convective losses showing maximum power that can be absorbed by the NW 24
Figure 4.1 An element with 2 nodes and 4 DOF 27
Figure 4.2 A beam with 3 elements/4 nodes and DOF 27
Figure 4.3 A cantilever beam with eliminated DOF at the clamped end 28
Figure 4.4 Classification of damping 30
Figure 4.5 (a) Variation of Young's *modulus with temperature; (b)*Young's *modulus, E (in Pa) along the non-dimensional length (ξ) of SiNW* 36
Figure 4.6 Variation of frequency with D/L^2 for stiffer (unheated NW with constant E) and softer (heated NW with distributed E) nanowires 37
Figure 4.7 Shift in Resonance frequency with amount of light absorbed by the SiNW 38
Figure 4.8 FRF of a NW at room temperature with different values of constant loss factor 39
Figure 4.9 Variation of amplitude with increase in loss factor (Q^{-1}). 40
Figure 4.10 FRF of NW with varying E and a distributed loss factor 41
Figure 4.11 FRF showing the difference between a constant and varying loss factors for nanowire with distributed Young's *modulus* 42
Figure 4.12 Comparison of stiffer NW with Softer NW 43
Figure 4.13 Change in amplitude of NWs with different Young's *modulus E* 44
Figure 5.1 Transverse vibrations of a beam in the x-y plane 46
Figure 5.2 Relative frequency shift due to absorption of laser power 53
Figure 5.3 For 2mW of laser power absorbed, (a) Variation in temperature of the NW and (b) Variation in *E* of the NW 55
Figure 5.4 Resonance shift due to attached mass at the tip of the cantilever 57
Figure 5.5 Resonance shift due to mass attached at different locations of the cantilever 58

Figure 5.6 Comparison of frequency shift due to attached mass using 4 methods 60

List of Abbreviations and symbols

Abbreviations

CTC	Circulating tumor cell
NW	Nanowire
SiNW	Silicon nanowire
NR	Nanoresonator
mW	milli-Watts
MHz	Mega Hertz
FRF	Frequency response function
E-B	Euler-Bernoulli

Symbols

Δf	Frequency shift (Hz)
Δm	Attached mass (Kg)
f_o	Initial frequency of the NW before heating (Hz)
m_o	Mass of the nanoresonator (Kg)
q_x	Conductive heat transfer rate in x-direction (W)
q_{conv}	Convective heat transfer rate (W)
q_{rad}	Radiative heat transfer rate (W)
k	Thermal conductivity (W/mK)
h	Convection coefficient (W/m^2K)
h_{rad}	Radiative heat transfer coefficient (W/m^2K)

A_c	Cross-sectional area of NR (m^2)
A_s	Surface area of NR (m^2)
T	Temperature of NR (K)
T_∞	Surrounding temperature (K)
Y	Non-dimensional temperature
ϵ	Emissivity ($0 < \epsilon < 1$) (Dimensionless)
σ	Stefan Boltzmann constant (W/m^2K^4)
P	Perimeter (m)
m	Fin parameter (m^{-1})
ξ	Non-dimensional length
L	Length (m)
$[M]$	Mass matrix (Kg)
x	Displacement vector (m)
$\ddot{x}$	Double derivative of x, acceleration (m/s^2)
f	Force/frequency (N/Hz)
$[K]$	Stiffness matrix (N/m)
E	Young's modulus (GPa)
I	Moment of inertia (m^4)
ρ	Density (Kg/m^3)
$\omega_r{}^2$	Eigenvalues - Angular frequency (rad/sec)
ψ	Eigenmodes
$\emptyset_r$	Mass-normalized mode shape for mode r
ζ	Damping ratio used to represent viscous damping

η	Loss factor used to represent structural damping
A	Amplitude
Q	Quality factor used to measure damping
$[C]$	Damping matrix (Viscous damping)
$[D]$	Damping matrix (Structural damping)
α	Frequency response function parameter - receptance
β_n	Frequency coefficient for mode ‘n’
ϑ	Deflection of beam

Acknowledgments

I am deeply thankful to my supervisor, Dr. Rustom Bhiladvala at the University of Victoria. By allowing me to pick my research topic, giving me the guidance I needed, and helping me through every step of the way, I grew self-confidence and a true passion for taking on new challenges. Thank you very much for your trust, your push, your energy, patience, your availability, your continuous support and encouragements.

I'd also like to express my sincere gratitude to Dr. Keivan Ahmadi, for giving me the opportunity to work with him. Thank you for your very valuable feedback and advice. I also wish to extend my thanks to my committee member Dr. Phalguni Mukhopadhyaya.

I'd like to thank my colleague Dr. Mahshid Sam, who has been my first point of contact during my research and for all her time and effort in explaining things clearly.

I'd like to thank my research group members Fan Weng, Amy, Jehad and Amin for all the fun moments we had, and the knowledge they shared with me. I'd like to thank Mostafa, Farzam, Hamed, and Gerrit for being there when I needed help with my Research calculations.

I'd like to thank all my friends, Suma, Venky, Monu, Ramz, Praneeth who are miles apart but still there for me in all the good and bad times of my life. I'd like to extend my thanks to Pranay, who walked with me through every moment of my life, since the day we met and made every complicated situation easy to handle.

A very special thanks to my Mumma who took care of me, supported me and loved me no matter what happened. I would have been nowhere today without her.

Dedication

To my beloved parents, my sister and my sweetest little nephew

Chapter 1: Introduction

1.1 Overview

Mechanical structures with small masses that vibrate at high frequencies have many applications in mass sensing [1]–[6], force sensing [7], biological [8], [9] and chemical sensing [10], [11]. These structures are referred to as resonators with promising applications in micro and nanotechnology [12].

A nanowire (NW) is a one-dimensional nanostructure with diameter in the range of nanometers and length in the range of nanometers to microns. Single nanowires have several applications in thermoelectrics [13], and field-effect transistors [14], [15]. Chained nanowires are used as transparent electrodes [16].

One of the most significant applications of nanowires as nanoresonators (NR) are considered in this thesis. A nanoresonator is a nanoscale object such as a beam, rod, or hollow tube, clamped at one or both ends. It is set to vibrate in a frequency range centered at one of its resonant frequencies. These resonant frequencies are also known as the normal modes of the resonator with a maximum vibration amplitude at resonance. Nanoresonators with picogram mass can attain a mass resolution in the attogram range.

A key element that is to be addressed in nanoresonators is the detection of their displacement. There are many experimental techniques for actuation and detection of a vibrating structures such as capacitive [17]–[20], piezo-electric [21]–[23] and electromagnetic [24] methods. Transduction is generally defined as the conversion of a signal from one form of energy to another. Transduction mechanism in nanoresonators is to be fully understood as the NRs vibrate at frequencies in MHz range, with small oscillation amplitudes in the range of nanometres. Optical transduction is the most widely used method that translates vibration of a nanoresonator into a measurable electric signal. However, detection by an optical method could influence the motion of the NR if energy from the laser beam focused on it for measurement causes a temperature increase in the NR. This thesis addresses the problem of the influence of laser light on the NR during resonance measurements.

The part of the effect of the laser on the mechanical properties of NR, known as the bolometric effect [25], includes the dependence of Young's modulus on temperature of the

resonator. Temperature distribution causes a frequency shift in the kHz range, which could reduce the mass resolution of NRs. In this thesis, we derive a method to first calculate the resonance frequency of a nanobeam with varying Young's modulus, and then use it to determine an effective Young's modulus for the NR beam.

1.2 Research Contributions

In mass sensing applications, the resonance frequencies are first measured for a bare beam and then again after mass addition. The added mass is calculated from the change in measured resonance frequency. The generated frequency signal should ideally depend only on the NW and the added mass. However, the influence of energy from the laser, coupled into the NR as thermal energy, could produce a significant error in resonance measurements. This requires an understanding of the effect of input laser power on resonance measurements.

The main objective of this research is to help obtain accurate conclusions from frequency measurements by quantifying and correcting for the effects of laser heating. This requires an understanding of factors influencing heat transfer, due to the small size of NWs and the resonance shift caused due to the laser heating effects.

The main contributions of this thesis are as follows:

1. The influence of laser power on temperature of the NW was studied. Using the heat equation, the temperature distribution in the NW was calculated for a range of fractions of laser power absorbed by the NW. It is shown from the calculations that 0.5 mW of laser power is enough to produce 200 K of temperature difference in the NW. Silicon NW tips could reach melting point with a few mW of laser power absorbed as heat.
2. Temperature distribution in the NW will influence its mechanical properties. This causes a downshift in resonant frequencies of the NW. Resonance calculations are made using numerical analysis in this thesis. Through our calculations, we quantify the resonance shift for the fundamental frequency and higher harmonics.
3. The analytical method to calculate the resonance frequency of a beam with constant stiffness is well-established. In this thesis, we derive a ***semi-analytical method*** to

calculate the resonance frequency of a beam with varying stiffness due to laser heating. The method is then extended to calculate the resonance frequency of the NR with a mass attached to the tip. The derived method is compared against four other methods of frequency calculations: ***Modal analysis, Euler-Bernoulli equation***, ***Blevins fundamental frequency equation,*** and the **1DOF *equation***

1.3 Thesis Structure

Chapter 2 consists of a review of the fabrication of NRs, actuation and detection techniques (transduction mechanisms) available in the literature, and an introduction of associated problems. It gives an overview of numerical modelling and finite difference methods used in the thesis.

Chapter 3 focuses on the effect of laser heating on nanowire. Finite difference simulations were carried out using MATLAB to calculate the temperature difference in Silicon nanowires for various fractions of laser power absorbed. This chapter presents the simulation results for temperature profiles based on convective and/or radiative losses, the effects of geometry and surrounding fluid on the behaviour of NW, and finally the maximum amount of laser power that can be absorbed by the NW. These are validated using the analytical results.

Chapter 4 focuses on resonance frequency shift due to laser heating. The amplitude of the resonance peak depends on the internal damping which is dependant on stiffness of the nanowire. This is calculated by considering assumed values of damping factor and its variation due to increase in temperature. This chapter presents the simulation results for resonance shift with varied amounts of laser power absorbed, amplitude with varying damping ratios and compare a stiff (unheated) and soft (heated) NWs.

Chapter 5 focuses on deriving a semi-analytical expression from Euler-Bernoulli framework to calculate the frequency of the heated nanowire with varying stiffness along its length. An effective Young's modulus value will be presented to serve as a correction factor for a given input laser power. This will be followed by the extension of the method derived to calculate resonance shift based on a mass attached to the nanowire.

Chapter 6 highlights the main conclusions of this thesis and recommendations for future work.

Chapter 2: Background and Literature Review

2.1 Overview

As mentioned in chapter 1, nanoresonators have many applications as mass sensors [1]–[6], force sensors [7], biological [8], [9] and chemical sensors [10], [11]. This chapter reviews the use of NRs in biological/mass sensing, and how they are fabricated in our lab to allow multiplexing (explained in 2.2.1). Another key element of NRs is the actuation and detection techniques which are reviewed, and the problems caused due to transduction mechanism involved are introduced. Chapter ends with the review of the numerical methods used in this thesis.

2.2 Role of NRs in biological sensing

NRs play a key role as biological sensors, which are used to detect Circulating tumor cells (CTCs) [26]–[28]. CTCs are cells that shed into the blood vessels from a primary tumor and are carried around the body during blood circulation. CTCs can potentially help in early detection of cancer. CTCs are captured using antibody-based methods targeting an epithelial cell adhesion molecule (EpCAM) [26]. However, EpCAM is not expressed by common types of cancer like breast cancer [27], [28]. In the research by Sioss et al [28], to detect diseases like cancer in early stages, they developed chips of metal or silica coated NWs to which antisense oligonucleotides are attached to detect RNA (purified by enrichment of CTCs from white blood cells) of various kinds of cancer. These RNA biomarkers are detected by measuring the resonance shift of the nanocantilever resonator due to added mass.

2.3 Fabrication of nanomechanical resonators

My colleague Dr. Mahshid Sam fabricated the nanoresonators in our research laboratory by developing a cost-effective field-directed assembly technique, to position the nanowires (NWs) on a large surface area. This fabrication technique is seen in the following sub-section.

2.3.1 Field-directed assembly of Nanoresonators (NR)

Top-down and bottom-up are two lithography techniques for micro and nanofabrication. Top-down methods are used to fabricate devices starting with larger dimensions etched to smaller desired structures. Photolithography, electron beam lithography, soft and nanoimprint lithography techniques come under top-down fabrication methods. Using these methods, devices with controlled shape and size can be fabricated [29], [30]. These methods require the removal of sacrificial area causing undercuts and underetching increasing compliance in nanoresonators [29], [30]. It also causes shape deterioration in cantilevers during its release while etching the sacrificial layer [29], [31]. Stress gradients in the device layer will result in the development of residual axial stresses in the doubly-clamped resonators [29], [32]. It is limited to the use of resonator material same as the clamping material.

Bottom-up methods corresponds to using of atoms or molecules for building multi-level structures. Atomic layer deposition and molecular self assembly are examples of these methods. Synthesizing the nanowires separately will have the benefits of preserving its reaction conditions without compromising other materials in the assembled device [33].

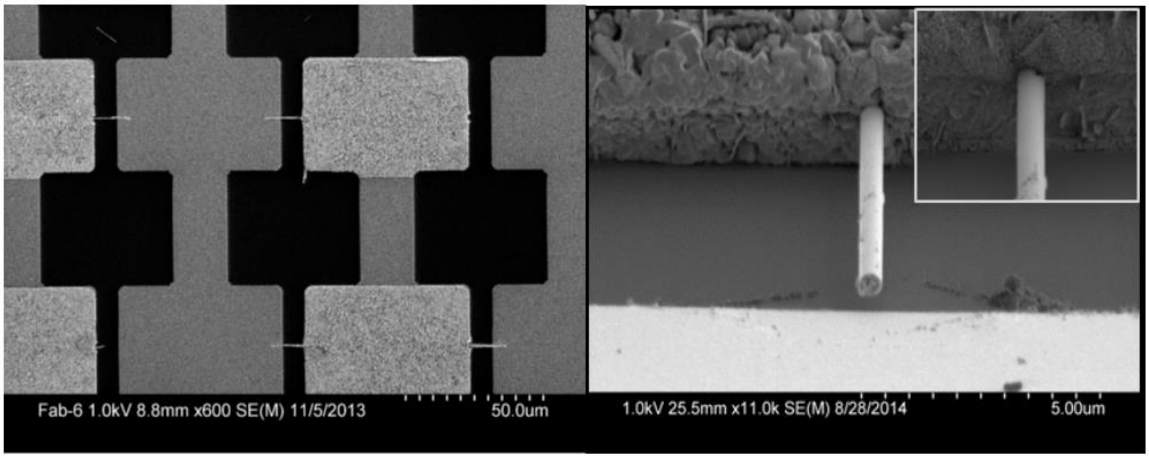

Figure 2.1 (a) Array of nanoresonators on the substrate fabricated by Field-directed method (b) Closer picture of one of the resonators on the substrate [16]

However, making larger arrays using self-assembly methods are very difficult in terms of clamping and addressing the nanowires individually [22].

Hybrid technique of field-directed assembly of nanowires combines the advantages of using photolithography from top-down and synthesis of nanowires off-the-chip by VLS method [21] from bottom-up methods [22]. This has the advantages of functionalizing NWs off-the-chip which has the ability of multiplexing, i.e., detection of various biomarkers by nanoresonators on the same chip [22], [29].

2.3.2 Other applications of Nanoresonators:

Nanoresonators are used as fluid damping sensors in the research by Bhiladvala et al [29], where the fluid damping and its effect on Q-factor of micro and nanoscale beams is studied by relating the Q-factor values in fluid and vacuum. Flow rarefaction regime was determined prior to calculating the fluid forces as the mean free path of gas molecules is larger than the beam's size. Fluid damping measurements with NWs can provide data for work in the transition regime where equations for continuum region or the free-molecular regime are no longer valid.

2.4 Nanoresonators (NR) for mass sensing

Nanomechanical resonators used in mass spectroscopy are crucial tools in chemical and biological industry. These nanoresonators with picogram masses are very sensitive to any mass attached to it. On adsorption of a mass to the resonator, its frequency downshifts accordingly (*Figure 2.2*), depending on the position of mass attached and geometry of the resonator [34]. And the relation between the frequency shift with change in effective mass is given as:

$$\frac{\Delta f}{f_o} = -\frac{1}{2}\frac{\Delta m}{m_o} \qquad [2.1]$$

Where f_o and m_o are the resonance frequency and mass of the nanowire before the added mass; Δm is the added mass and Δf is the frequency shift caused by the added mass.

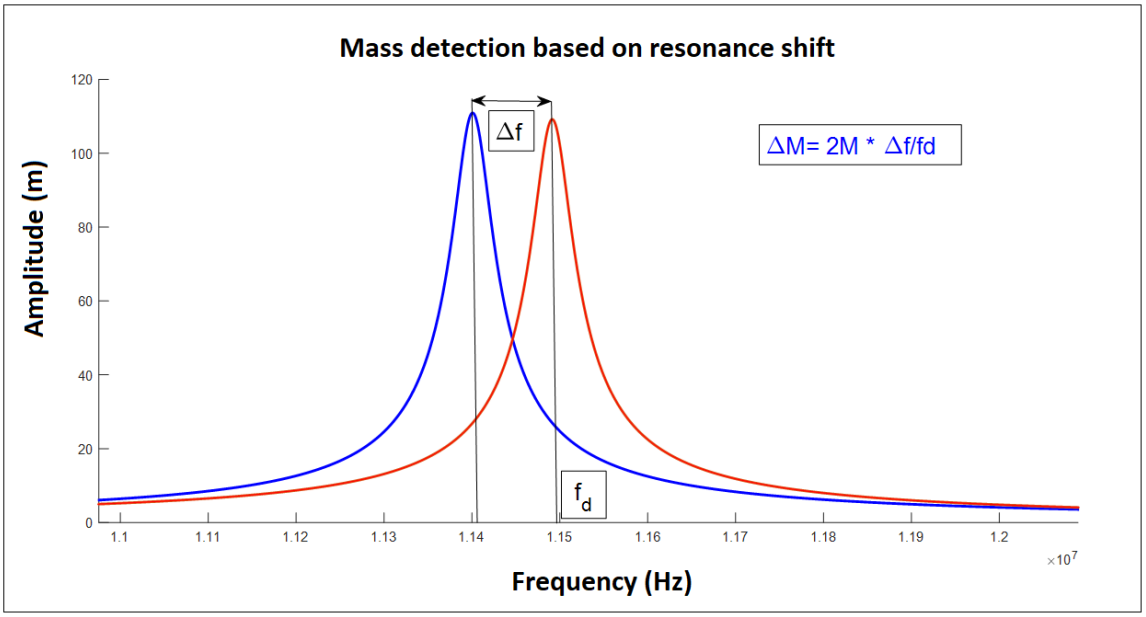

Figure 2.2 Resonance downshift due to attached mass

Different techniques can be used for nanowire actuation which is seen in the following sub-section.

2.4.1 Actuation and detection techniques

Micro/Nano electromechanical devices are actuated based on various mechanisms such as electrostatic (capacitive) [17]–[20], electromagnetic [24], thermal [17], [35] and piezo-electric effects [21]–[23].

Magnetomotive actuation: Sensor is placed in a magnetic field and an alternating current (AC) field is driven across it. This generates Lorentz force actuating the sensor. This is detected by the variation in flux with time which induces an electromotive force (EMF) in the loop [17]. Depending on the nanowire orientation with respect to the magnetic field, vibration can be in-plane or out-of-plane direction.

Capacitive actuation: The basic principle of this method operates by considering an elastic conductive resonator on top of a rigid perfect conductor. When an AC voltage is applied to the resonator, it imposes variation of charge in both the conductors and are attracted to each other. It is detected by the change in capacitance, when the distance between the two conductors change.

Piezoelectric actuation: It works on the principle of inverse piezoelectric effect, i.e., when an electric voltage applied to the piezoelectric material, it generates stress. Contraction and expansion of the piezoelectric material under an applied AC signal, generates a vibrational force to the actuator. In our lab, indirect method is used, where a commercial piezoelectric disk is bonded to the substrate of resonators which move with each other.

Thermal actuation: In this method, bilayer structures with different thermal expansion coefficients are considered. When the structure is heated, it is subjected to stress due to varied thermal expansion in them, causing an actuating force.

Magnetostrictive actuation: This is caused by a dimensional change in the magnetic material due to change in the magnetic state of the sensor.

For detection of cantilever deflection, optical method [36]is the most widely used method and interferometric methods [7] are used in precise measurements. Optical transduction works on the principle that the intensity of reflected light varies with vibration of the resonator and is explained by Favero et al [37], using two mirrors attached by a spring and the cavity being probed by a laser. Measurement setup in our lab for optical transduction is explained in the following section.

2.4.1.1 Optical transduction method for resonance measurement

In this method, nanoresonators are placed in a vacuum chamber and is secured on an inverted optical microscope. A spectrum analyzer is used to generate an RF electric signal to drive the piezo disk underneath the chip, making it vibrate at its resonant frequencies. Then, a 10 mW He-Ne laser of wavelength 633 nm is focused on to the tip of the vibrating nanowire on the chip, providing about 4 mW of input power for the measurement purpose. Light reflected off the vibrating nanowire passes back through the photodetector and is analyzed by the spectrum analyzer to generate a frequency signal.

Optical transduction method is used for measuring the resonance frequency of cantilever resonators by Belov et al [38], and doubly-clamped resonators by Ekinci et al [3] in the literature.

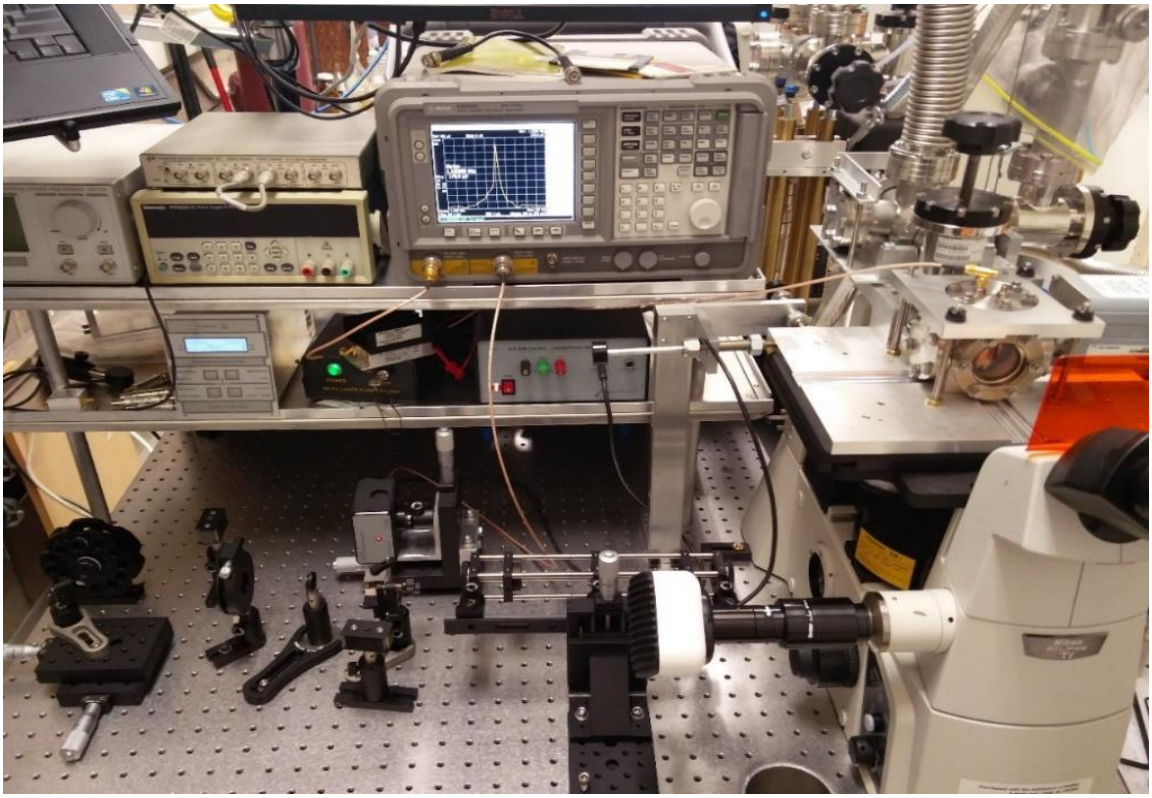

Figure 2.3 Optical measurement setup [30] displaying a frequency signal on spectrum analyser when laser is focused on the NW

2.4.2 Resonance shift due to laser heating

The sensitivity of optical measurement setup is limited by the noise sources. Photodiode shot noise and the Johnson noise are the two major noise sources in the optical measurement setup which can be reduced by increasing the output power of the laser diode [39]. Therefore, it is appealing to use higher powers of laser using a neutral density filter to improve the signal-to-noise ratio (SNR). Schematic of optical measurement setup is shown in *Figure 2.4*.

In the experiments conducted by Weng Fan [23] in our lab, using this optical measurement setup shown in *Figure 2.3*, he generated a frequency signal with varying inputs of laser

power and has observed a downshift in the resonance frequency as the laser power is increased (*Figure 2.5*).

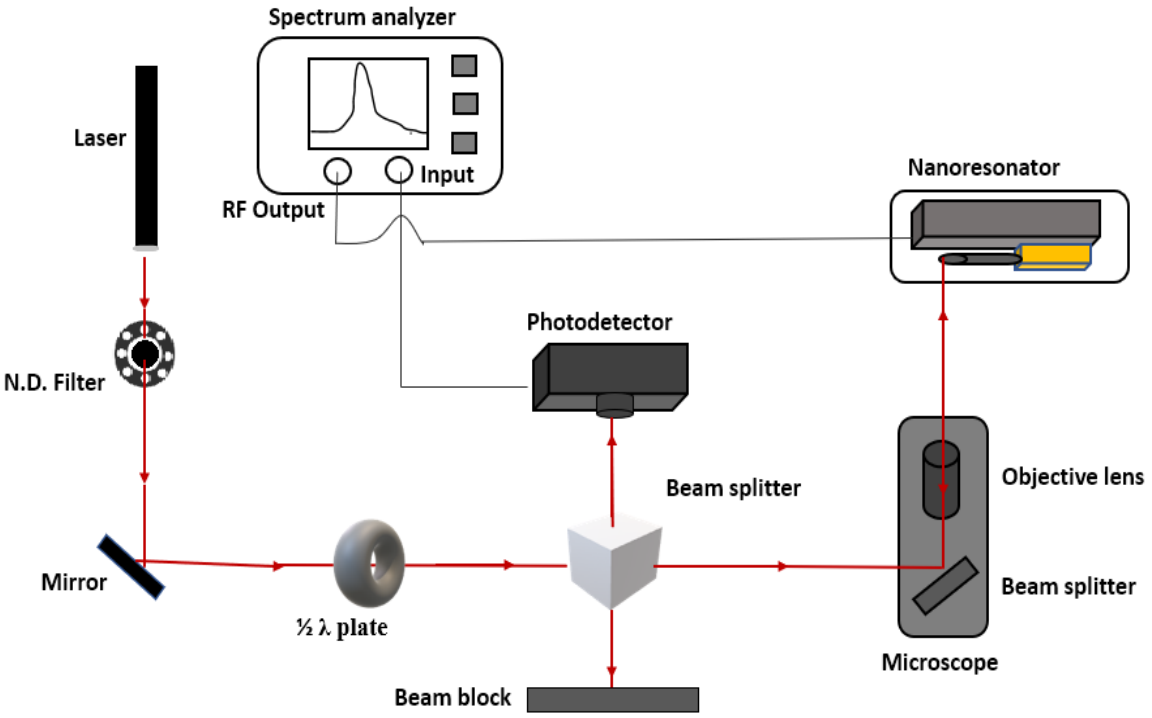

Figure 2.4 schematic of optical measurement setup

Similar effects of resonance shift due to increase in laser power has been observed in experiments by several researchers in their experiments [40]–[42]. This shift in the resonance is due to absorption of light focused on tip of the nanowire (NW) by the NW itself which is explained in chapter 3.

F.A. Sandoval et al [42] have presented an experimental evidence on micro cantilevers for resonance downshift due to increase in laser power. They reported values of tip temperatures of the NW based on resonance shifts. They also reported cantilevers reaching its melting point for a few mW of laser power with conduction as the only thermal transfer process in vacuum, as the NW softens with increase in temperature, i.e. decrease in Young's modulus.

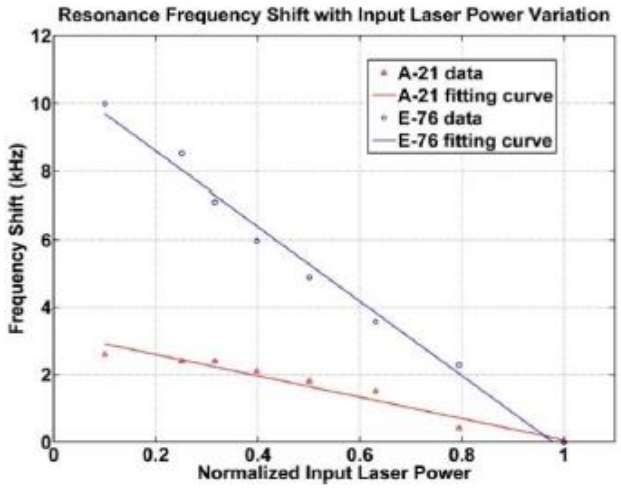

Figure 2.5 Downshift of resonance frequency with increase in laser power [30] with A-21 and E-76 in the sub plot showing different Rhodium resonators on the same substrate

However, T. Sahai et al [43] conducted experiments on doubly-clamped micro oscillators and observed a softening-hardening transition behaviour as the laser power is increased in the process of improving the SNR of the frequency signal.

2.5 Finite difference Methods (FDM)

This thesis considers the finite difference model of the nanowire to numerically calculate the temperature of the nanowire with given amount of laser absorbed by the nanowire. For a 4 mW of total input power focused on the NW, it is assumed that a 40% of the input laser (from 0 to 4 mW) is absorbed by the NW, based on the ratio of NW diameter to the laser beam spot size. This thesis does not present calculations of thermal energy laser absorbed by the NW, as its dependence on several factors like diameter of NW, optical properties of Silicon, plane of polarization and wavelength of laser are not well understood.

After the temperature calculations, a numerical model of the NR is considered to calculate the change in resonance frequency of the NW due to the temperature attained by it, which causes a change in Young's modulus of the NW. The derived semi-analytical Euler-Bernoulli method for a beam of varying Young's modulus is used to validate the resonance

shift results. This method is further extended to calculate the resonant frequency of a beam with a lumped mass attached to the tip of the NW.

Chapter 3: Numerical Model for Temperature Analysis of a Laser Heated Nanowire

As discussed in optical transduction setup in Chapter 2, laser is focused on NW during frequency measurements. The light reflected off the NW is guided to photodetector where an electric signal is generated and analyzed by spectrum analyzer to generate a frequency curve. However, the sensitivity of the optical setup depends on the shot-noise of photodetectors. Photodiode shot noise is a major noise source in the optical measurement setup which can be reduced by increasing the output power of the laser [39]. So higher intensities of light are appealing to obtain a better signal-to-noise ratio.

However, a part of the laser power is absorbed by the NW as heat. This can reduce the mass resolution of NWs and may also cause permanent deformation. The heating of NWs depends on many factors, such as the intensity of light, fraction of light absorbed as thermal energy, the thermal conductivity of NW, the dimensions of the NW and the heat dissipated through the NW. Silicon nanowires have a large absorption efficiency with only 37% of reflection [44]. Absorption depends on wavelength of light [45], diameter of NW [45], [46], angle of incident light [46], and plane of polarization of light [46], [47]. Therefore, thermal transport in NWs is a critical issue which needs to be studied.

This chapter focuses on the numerical study of interaction between laser and SiNWs to calculate the temperature distribution using a heat equation. The analysis is carried out by solving a Fourier heat equation inside a laser heated NW. NW temperature is determined by different factors: Intensity of laser, assumed fraction of laser absorption, dimensions of NW, thermal conductivity as a function of temperature. The calculations are done for a NW in vacuum.

3.1 Computational analysis for determining the temperature profile of nanowire

3.1.1 Theoretical modelling of heat transport in SiNWs

One-dimensional cylindrical Silicon nanowire (SiNW) which is 6 microns in length, and 400 nanometers in diameter, is analyzed using a model in which some

assumptions of fin heat transfer are applicable. All the calculations in this thesis are made using the same dimensions mentioned, unless otherwise mentioned.

The SiNW is initially at room temperature, clamped to the substrate at one end and free at other (cantilever). As seen in *Figure 2.1(b),* the gold mounting pedestal for our NWs made by field-directed assembly has a large thermal mass, high thermal conductivity and makes intimate contact around the NW periphery. The pedestal temperature is therefore assumed to be a heat sink or reservoir at close to room temperature. The temperature of the surroundings is assumed to be 298 K. In experiments, a Helium-Neon laser (λ=633.2 nm and 4mW max power) is used, with controllable power setting, with the laser focused on the tip of the nanowire as shown in the *Figure 3.1*.

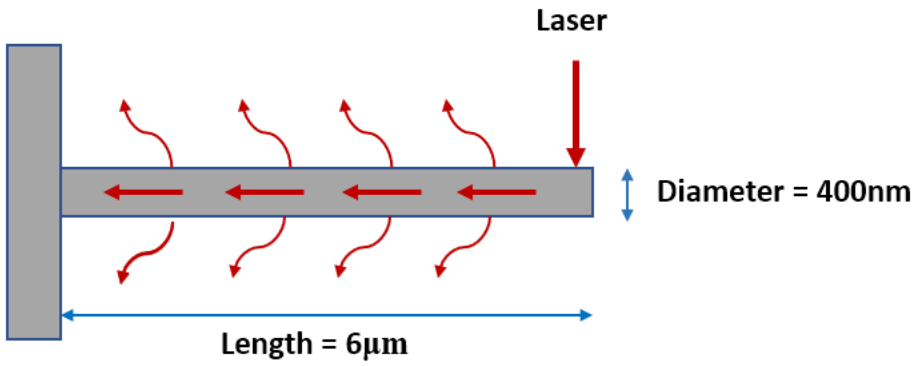

Figure 3.1 Silicon Nanowire description

For our calculations, we consider a range of values, from 0 to 2.6 mW, for thermal energy injected into the free tip of the NW.

3.1.2 Governing equations for Heat Transfer inside the Nanowire

Considering a NW in a vacuum chamber and the laser beam as a heat source supplying heat at the tip of the NW, the equation governing heat transfer is derived from the energy balance shown in the *Figure 3.2* below. Heat is dissipated in the NW by conduction and radiation. However, calculations for convection are also shown for a wire assumed to have a convection co-efficient of 25 W/m^2K to compare the effects of convection and radiation.

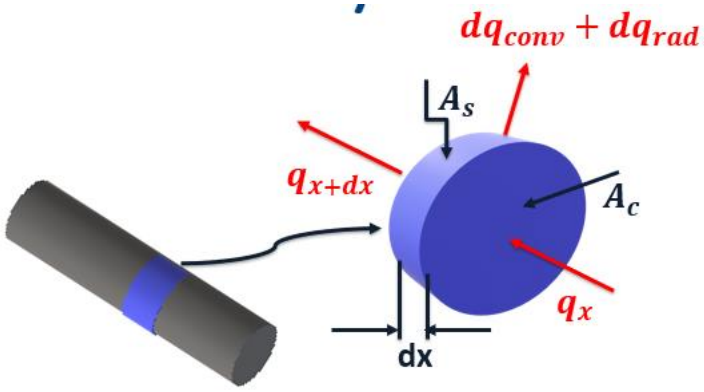

Figure 3.2 Energy Balance in NW

To analyze conduction of heat through the NW, we can calculate the heat transfer rate from Fourier's law [68] as shown below:

$$q_x = -kA_c \frac{dT}{dx} \quad [3.1]$$

Where, $'q_x'$ is the rate of heat transfer in x-direction. $'k'$ is the thermal conductivity of Silicon at room temperature which is 148 W/mK. $'A_c'$ is the cross-sectional area of SiNW and $'T'$ is the surface temperature.

$$q_{conv} = hA_s\,(T - T_\infty) \quad [3.2]$$

$'q_{conv}'$ is the convective heat transfer rate. $'h'$ is the coefficient of convective heat transfer. $'A_s'$ is the surface area of the NW. $'T_\infty'$ is the surrounding temperature [68].

$$q_{rad} = \epsilon\sigma A_s(T^4 - T_\infty^4) \quad [3.3]$$

$'q_{rad}'$ is the radiative heat transfer rate. $'T_\infty'$ is the surrounding temperature.$'\epsilon'$ is the emissivity. $'\sigma'$ is the Stefan Boltzmann's constant which is equal to [68]:

$$\sigma = 5.67 * 10^{-8}\, W/m^2K^4 \quad [3.4]$$

From the energy balance:

$$q_x = q_{x+dx} + dq_{conv} + dq_{rad} \quad [3.5]$$

From Taylor's series expansion, we have:

$$q_{x+dx} = q_x + \frac{dx}{1!}\frac{dq_x}{dx} + \frac{dx^2}{2!}\frac{d^2q_x}{dx^2} + \frac{dx^3}{3!}\frac{d^3q_x}{dx^3} + \cdots, \qquad -\infty < x < \infty \quad [3.6]$$

By substituting Eq. (3.6) in Eqns. (3.1), (3.2), (3.3) & (3.5), we get the heat equation as:

$$\frac{d}{dx}\left\{kA_c\frac{dT}{dx}\right\} - h\frac{dA_s}{dx}(T - T_\infty) - \epsilon\sigma\frac{dA_s}{dx}(T^4 - T_\infty^4) = 0 \quad [3.7]$$

By dividing the whole equation with k and taking A_c as a constant, we get:

$$\frac{d^2T}{dx^2} + \left(\frac{1}{k}\frac{dk}{dx}\right)\frac{dT}{dx} - \frac{hP}{kA_c}(T - T_\infty) - \frac{\epsilon\sigma P}{kA_c}(T^4 - T_\infty^4) = 0 \quad [3.8]$$

Introducing the dimensionless parameters and the fin parameter *m*:

$$T(x = 0) = T_b, \qquad Y = \frac{T(x) - T_\infty}{T_b - T_\infty}, \qquad \xi = \frac{x}{L} \quad [3.9]$$

$$Fin\ parameter, m = \sqrt{\frac{hP}{kA_c}}\ (units\ m^{-1})$$

The final equation in the non-dimensional form is given by:

$$\frac{d^2Y}{d\xi^2} + \left(\frac{1}{k}\frac{dk}{d\xi}\right)\frac{dY}{d\xi} + \left[\left(-\frac{hPL^2}{kA_c}\right) + \left(-\frac{\epsilon\sigma PL^2T_\infty^3}{kA_c}\left\{\left(\frac{T}{T_\infty}\right)^3 + \left(\frac{T}{T_\infty}\right)^2 + \left(\frac{T}{T_\infty}\right) + 1\right\}\right)\right]Y = 0 \quad [3.10]$$

This equation is simplified as:

$$\frac{d^2Y}{d\xi^2} + \left(\frac{1}{k}\frac{dK}{d\xi}\right)\frac{dY}{d\xi} + \left[\left(-\frac{hPL^2}{kA_c}\right) + \left(-\frac{h_{rad}PL^2}{kA_c}\right)\right]Y = 0 \quad [3.11]$$

Where,

$$h_{rad} = \epsilon\sigma T_\infty^3\left\{\left(\frac{T}{T_\infty}\right)^3 + \left(\frac{T}{T_\infty}\right)^2 + \left(\frac{T}{T_\infty}\right) + 1\right\} \quad [3.12]$$

$'h_{rad}'$ is an equivalent radiative heat transfer coefficient which is strongly dependant on temperature.

$$\frac{d^2Y}{d\xi^2} + (H(\xi))\frac{dY}{d\xi} + r(\xi)Y = 0 \quad [3.13]$$

Where,

$$H(\xi) = \frac{1}{k}\frac{dK}{d\xi} \quad [3.14]$$

$$r(\xi) = -\frac{hPL^2}{kA_c} - \frac{\epsilon\sigma PL^2T_\infty^3}{kA_c}\left\{\left(\frac{T}{T_\infty}\right)^3 + \left(\frac{T}{T_\infty}\right)^2 + \left(\frac{T}{T_\infty}\right) + 1\right\} \quad [3.15]$$

3.1.3 Discretization of governing equations and boundary conditions:

The mesh implemented consists of *N* intervals with *N+1* nodes and length of each interval is given by $\Delta\xi = \frac{1}{N}$. A description of the domain with N intervals is given as:

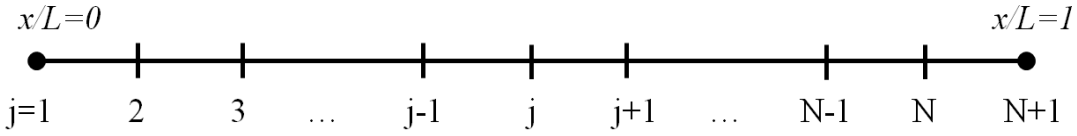

Figure 3.4 Discretization of mesh in to N intervals

In order to solve the governing equations numerically, derivatives of *y* in *Equation 3.13* are represented using the central differences as:

$$\frac{d^2Y}{d\xi^2} = \frac{Y_{j+1} - 2Y_j + Y_{j-1}}{\Delta\xi^2} \quad [3.16]$$

$$\frac{dY}{d\xi} = \frac{Y_{j+1} - Y_{j-1}}{2\Delta\xi} \quad [3.17]$$

Finite difference expression method (FDM) is used to compute the temperature distribution across the NW. Equation (3.13) is expanded using central difference approximation as:

$$\frac{Y_{j+1} - 2Y_j + Y_{j-1}}{\Delta\xi^2} + H_j\,\frac{Y_{j+1} - Y_{j-1}}{2\Delta\xi} + r_jY_j = 0 \quad [3.18]$$

H_j & r_j are calculated using Eqns. (3.14) & (3.15). By re-arranging the coefficients, we get the following equation:

$$\left(1 - H_j\,\frac{\Delta\xi}{2}\right)Y_{j-1} + (-2 + r_j\Delta\xi^2)Y_j + \left(1 + H_j\,\frac{\Delta\xi}{2}\right)Y_{j+1} = 0 \quad [3.19]$$

This can be written as:

$$c_jY_{j-1} + a_jY_j + b_jY_{j+1} = d_j \quad [3.20]$$

Where,

$c_j = 1 - H_j\,\frac{\Delta\xi}{2}$;

$a_j = -2 + r_j\Delta\xi^2$

$b_j = 1 + H_j\,\frac{\Delta\xi}{2}$; & $d_j = 0$

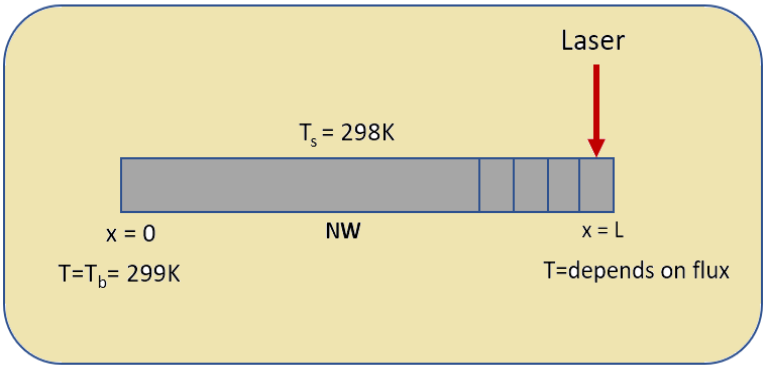

Figure 3.3 Laser focused on tip of the NW showing BC's

As discussed in earlier sections, one end of the nanowire is considered to be at 299K and temperature on the other end depends on intensity of the laser or the heat flux (as shown in (*Figure 3.3*).

Non-dimensional temperature at $\xi = 0$ is given by:

$$Y(0) = Y(\xi = 0) = 1 \qquad [3.21]$$

Since the laser power is being conducted through the NW, non-dimensional temperature gradient at $\xi = 1$ is given by the conduction equation:

$$\left.\frac{dY}{d\xi}\right|_{\xi=1} = \frac{-q}{kA_c} * \frac{L}{T_b - T_\infty} \qquad [3.22]$$

Using the backward differences with fourth degree accuracy ($\Delta\xi^4$), we can write by expanding Taylor's series as:

$$\left.\frac{dY}{d\xi}\right|_{\xi=1} = \frac{11Y_{N+1} - 18Y_N + 9Y_{N-1} - 2Y_{N-2}}{6\Delta\xi} \qquad [3.23]$$

From *Equations (3.22) & (3.23)*, we have:

$$\frac{-q}{kA_c} * \frac{L}{T_b - T_\infty} = \frac{11Y_{N+1} - 18Y_N + 9Y_{N-1} - 2Y_{N-2}}{6\Delta\xi} \qquad [3.24]$$

Heat transfer rate, q depends on the input laser power and the fraction of it being absorbed by the NW which can be given as:

$$q = I * f \qquad [3.25]$$

where, I is the intensity of laser power and f is the fraction of laser power absorbed by the NW. f depends on the factors like wavelength of light, material and diameter of the nanowire, diameter of laser spot, angle of incident light and plane of polarization. However, in this case it is assumed that 40% of it is assumed by the NW based on diameters of laser spot and NW of 1μm and 400nm respectively.

3.1.3.1 Temperature distribution in case of Radiation and its dependence on mesh size

To calculate the temperature distribution of the NW in the radiative environment, temperatures (Y_j) calculated in the case of convection are taken as a first guess to solve for final temperatures $Y_j^{(1)}$. Then the coefficients c_j, a, b_j & d_j are re-evaluated to solve for temperatures $Y_j^{(2)}$ and the process is repeated until the values of temperature converge, i.e. $\left|1 - \frac{y_j^{(k)}}{y_j^{(k+1)}}\right| \leq tolerance$. Where the $tolerance = 10^{-n}$ and the value of n depends on $\Delta\xi$. If $\Delta\xi = 10^{-n}$, then $tolerance = 10^{-4}$.

Since radiation has a 4th degree temperature term, it is highly non-linear and when we try to linearize it using a difference method, results are highly unstable with a large mesh size. The mesh should be refined and checked for instability. In this simulation, the mesh size is at least 20 times smaller in the case of radiation compared to convection for lower laser intensities.

3.1.4 Thomas Algorithm

Equation (3.20) was solved using the Thomas algorithm. This is a Tri-diagonal matrix algorithm which is a simplified form of Gauss elimination. This algorithm starts with forward elimination, getting rid of one of the unknowns from each equation and ends with backward substitution to calculate the vector of unknowns.

3.2 Simulation Results and Discussion

The aforementioned expressions are implemented using MATLAB (programs are listed in the appendices). Results discussed below show the effects of variation of thermal conductivity as a function of temperature, as well as convection and radiation from the NW

surface. As mentioned earlier, the absorption of laser power is assumed in this thesis, from zero to the maximum, where a part of the NW reaches its melting point.

3.2.1 Linear profile of the NW with constant conductivity in the case of convective losses

Figure 3.4 is the temperature profile of the NW for a 2mW rate of thermal energy input from the laser. The profile was generated in MATLAB using a Neumann boundary condition (constant heat flux BC). Conduction and convection are the thermal processes considered in this simulation. Thermal conductivity is taken as constant in this case. We note that, this is done only to compare the effects of convection and radiation later in the chapter, but there is no convection acting when the NWs are in a vacuum (MATLAB code for this simulation is given in Appendix A).

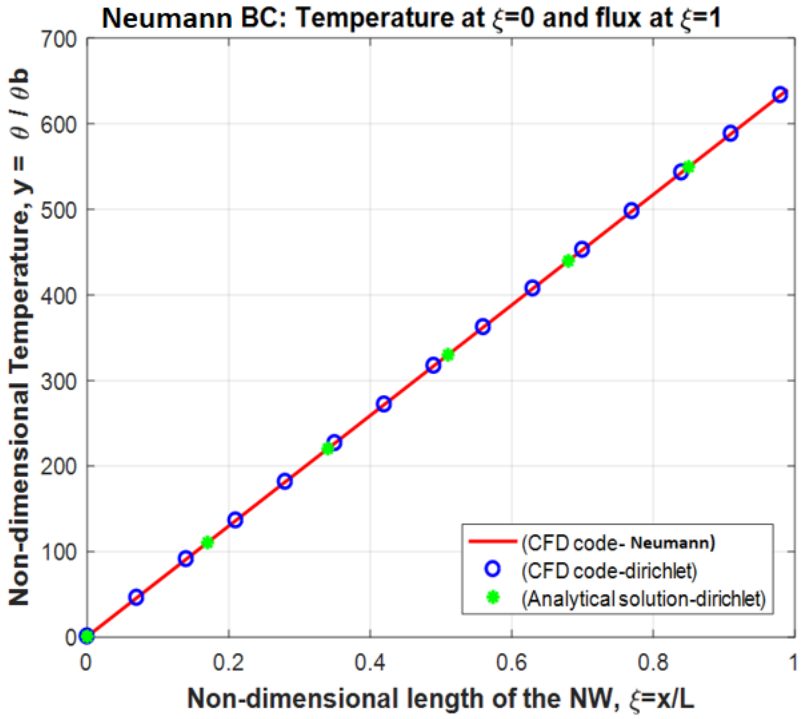

Figure 3.4 Linear temperature profile of SiNW with convective losses

This simulation was checked and found to be in agreement with simulations and analytical solution (given in Appendix B) using a Dirichlet BC (specified temperature value at tip). For these checks, the temperature at the tip was taken from the earlier Neumann BC simulation.

In *Figure 3.5* (a), the radius of the NW is reduced to increase the surface area over the cross-section. It is seen that the effect of convection becomes pronounced for values of $mL \geq 2$. The term mL is defined in *Equation (3.9).*

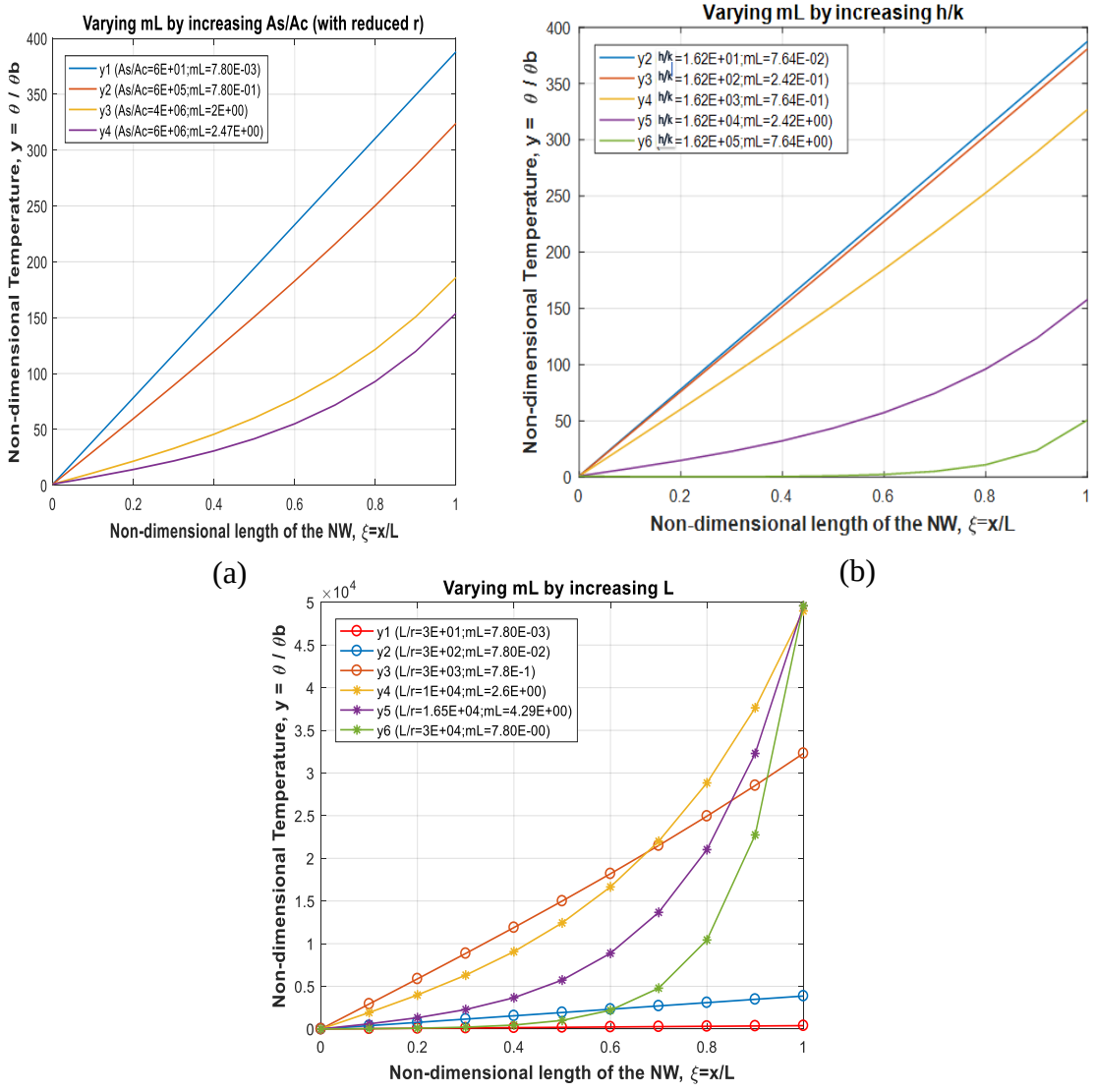

Figure 3.5 Varying the values of mL to make the profile non-linear by: (a) Increasing the h/k ratio (b) Increasing the surface area by reducing radius of the NW (c) Enhancing the aspect ratio by increasing length of the nanowire

This plot is generated to show the dominance of conduction over convection at nanoscale and the importance of mL acting as a stretching factor. Similarly, in *Figure 3.5*

(b) & (c) convective coefficient and length of the NW are increased respectively until the *mL* reaches a value of 2, to see the effects of convection.

3.2.2 Variation in thermal conductivity of Si with temperature

Thermal conductivity decreases with temperature for any material. Values in *Figure 3.6* are taken from the literature [53], [54] from room temperature to the melting point of silicon and plotted to find the equation for the best fit curve. There will be a significant difference in heat transfer when the thermal conductivity is not taken to be a function of temperature, as will be shown in the Section 3.2.4.

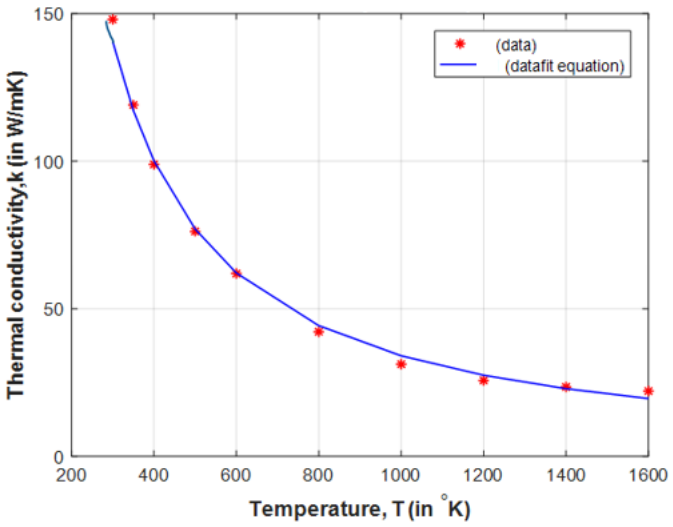

Figure 3.6 Variation of Thermal conductivity with temperature

The best fit equation to the data for variation of thermal conductivity (k, in W/m.K) of Silicon with temperature (T, in K) is given as:

$$k = 115598 * T^{-1.177} \qquad [3.26]$$

3.2.3 Non-linear temperature profile with variable thermal conductivity for cases of convection and radiation

Figure 3.7 (a) and (b) allow comparison of temperature profiles with convective losses and radiative losses, respectively, from the NW, for 2mW of absorbed laser power. Although the equivalent heat transfer coefficient value for convection is less than half that for radiation (after convergence of the non-linear temperature-dependent solution) we observe that the effects of radiation and convection are almost indistinguishable in the temperature profile plots. This suggests that the non-linearity in profile is due primarily to the thermal conductivity variation with temperature. The radiative or convective loss was found to be about 1% of heat transport by conduction, by comparing tip temperatures for:

(1) conduction only

(2) conduction & convection

(3) conduction & radiation.

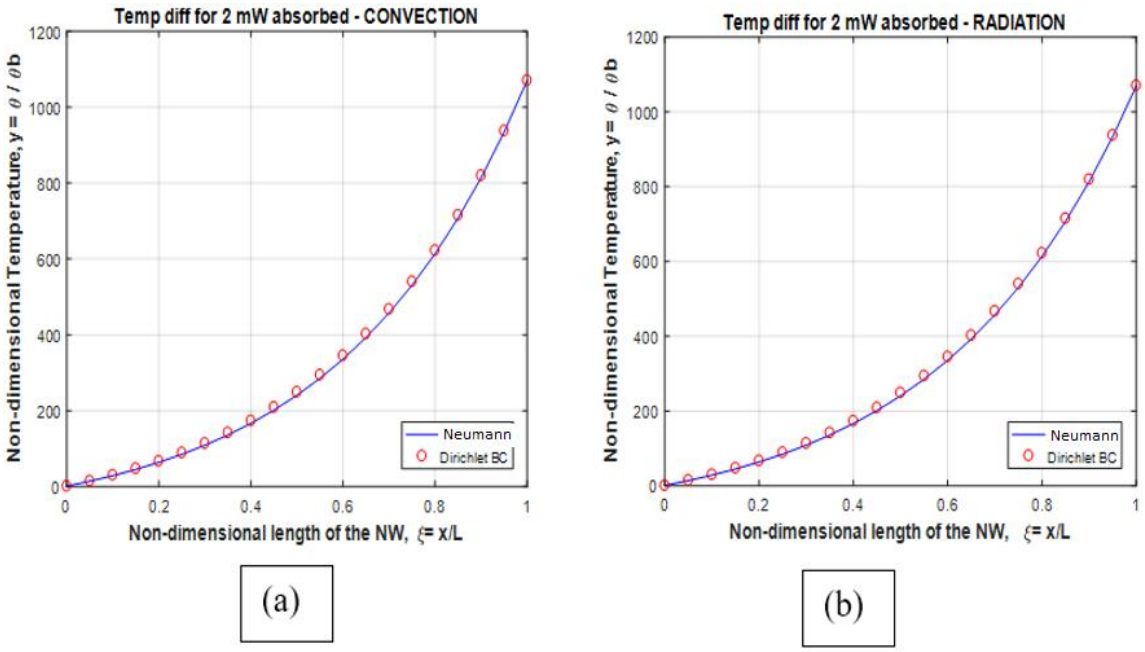

Figure 3.7 Temperature profile with: (a) convective losses at 2mW of power absorption (b) radiative losses at 2mW of power absorption by Si NW

3.2.4 Maximum power that could be absorbed by the NW

As discussed earlier in the chapter, the fraction of laser power absorbed as heat by the NW determines the temperature reached by the NW.

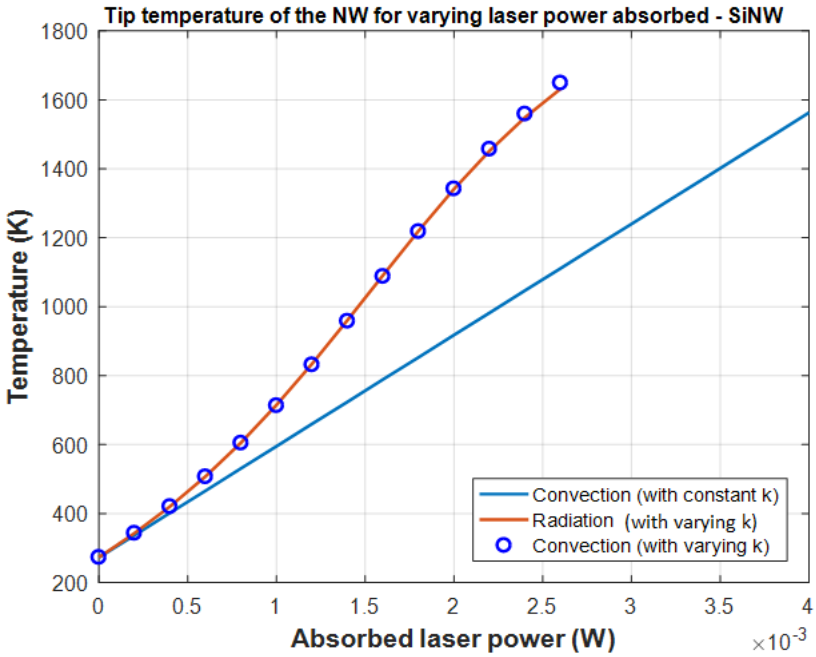

Figure 3.8 Tip temperatures vs absorbed laser power by SiNW with radiative/convective losses showing maximum power that can be absorbed by the NW

Figure 3.8 shows the tip temperatures of the NW calculated for the following conditions: (1) Convection and radiation with varying thermal conductivity and (2) Convection with constant thermal conductivity. This figure conclusively shows that there is a significant difference in profiles with and without considering the variation of thermal conductivity as a function of temperature.

It is also seen that the effect of radiation and convection are nearly equal which can be explained in terms of equivalent $\boldsymbol{h_{rad}}$, i.e., $\boldsymbol{h_{rad}} = \left(\boldsymbol{\epsilon\sigma T_\infty^3}\left\{\left(\frac{T}{T_\infty}\right)^3 + \left(\frac{T}{T_\infty}\right)^2 + \left(\frac{T}{T_\infty}\right) + 1\right\}\right)$. This value represents radiation using an equivalent temperature-dependent heat transfer coefficient. As shown in figure 3.5, the value of (h/k) should be at least be $\boldsymbol{1.6 * 10^4}$ m^{-1} to see the effects of convection. With free convection heat transfer values h =25 W/m^{2}K and radiation-equivalent value (after convergence) h_{rad} = 64 W/m^{2}K will yield values of h/k far smaller than $\boldsymbol{1.6 * 10^4}$. With all these factors considered, the maximum amount of laser power that can be absorbed by the NW before it melts, is calculated to be 2.6 mW as seen in *Figure 3.8*.

3.2.5 Other thermal considerations at nanoscale

Natural convection depends on buoyant force due to temperature difference and on the viscosity of surrounding air [48], [49]. However, buoyancy is negligible at nanoscale, as the interaction of air with the NW is based on a few individual interactions of the molecules in the air with the surface of the NW [50]. Knudsen number defined as the ratio of mean free path over characteristic length, influences the convective heat transfer at nanoscale. At high Knudsen numbers, viscous shear stress and convection are both greatly reduced, as there are far fewer molecules colliding with each other [51], [52].

Radiation at nanoscale is also a focus of current research. When NW diameters are much smaller than the wavelength of blackbody radiation estimated from Wien's Law, there will be significant deviations in view-factor dependent radiation calcuations [55]. For instance, if there are NWs at a distance of 1-2 microns, the thermal link between them can be quite strong because there is a coupling of the evanescent EM waves (near-field effects) [55], [56].

However, the size effect dominates if the surface area of the NW is too small and the thermal transport is then dominated by conduction.

3.3 Conclusions and Recommendations

This chapter dealt with the heat equation to determine the temperature profile of a laser heated NW. All the equations were implemented in MATLAB using finite difference methods and are validated using numerical and analytical equations for Dirichlet BC.

It is seen in the chapter that the conduction is dominant over convection/radiation at nanoscale and thermal conductivity variation with temperature is an important factor to be considered. The linear temperature profile is explained in terms of the value of the non-dimensional term, mL, which serves as a stretching factor and should at least be equal to 2 for the temperature profile to be non-linear. With these factors considered, the maximum laser power that can be absorbed by the NW before a part of it melts, is calculated to be 2.6 mW. These calculations could help in determining the optical absorption in NWs.

Since the laser beam exhibits a Gaussian power profile, excitation will depend on the position of the NW inside the laser spot. Hence, it is recommended to study the effects of position of NW within the laser spot, in future studies.

Chapter 4: Resonance Shift due to Laser Heating

This chapter deals with resonance calculations by solving equations of motion based on spring-mass-damper system. This gives an overview of vibrational analysis which progresses in three phases [57]:

i. Spatial model: Describes the structure's physical properties such as mass *M*, stiffness *K* and damping properties.
ii. Modal model: Gives a set of natural frequencies ($\bar{\omega}_r^2$) with corresponding modal damping ratios and vibration mode shapes(ψ).
iii. frequency response functions (FRF): Analyses how structures respond under given harmonic excitation conditions and with what amplitudes.

This begins with calculating eigenvalues and eigenvectors of an undamped model followed by similar calculations of a structurally damped model. These are done, first, to calculate the change in resonance frequency of laser heated nanowires, and second, to see how damping affects vibration amplitude of the NW. At the end, initial stiffer (unheated) NWs will be compared with laser heated (softer) NWs to show how laser heating influences resonance measurements.

4.1 Undamped multi degrees of freedom (MDOF) system:

Equation of motion for an undamped MDOF system, with N degrees of freedom, is solved to determine eigenvalues and eigenvectors:

$$[M]\{\ddot{x}(t)\} + [K]\{x(t)\} = \{f(t)\} \qquad [4.1]$$

where [*M*] and [*K*] are NxN DOF mass and stiffness matrices; $\{x(t)\}$ & $\{f(t)\}$ are Nx1 vectors of time-varying displacements and forces. Let us consider a beam finite element model, with 1 element and 2 nodes, having 2 DOF (displacement and slope) on each side of the node as seen in the *Figure 4.1*:

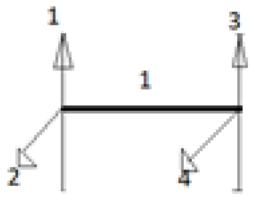

Figure 4.1 An element with 2 nodes and 4 DOF

The consistent stiffness matrix [*K*] for translational inertia in a prismatic beam shown in the *Figure 4.1* is given by:

$$K = \frac{2EI}{L^3}\begin{bmatrix} 6 & 3L & -6 & 3L \\ 3L & 2L^2 & -3L & L^2 \\ -6 & -3L & 6 & -3L \\ 3L & L^2 & -3L & 2L^2 \end{bmatrix} \qquad [4.2]$$

where *E* is the Young's modulus of the material being used, *I* is the moment of inertia and *L* is the length of the beam.

Similarly, the consistent mass matrix [*M*] for translational inertia in a prismatic beam is given by:

$$M = \frac{\rho AL}{420}\begin{bmatrix} 156 & 22L & 54 & -13L \\ 22L & 4L^2 & 13L & -3L^2 \\ 54 & 13L & 156 & -22L \\ -13L & -3L^2 & -22L & 4L^2 \end{bmatrix} \qquad [4.3]$$

Here, ρ is the density, and *A* is the cross-sectional area.

Similarly, for a beam with 3 elements/4 nodes having 8 DOF, the assembled stiffness and mass matrices are given by:

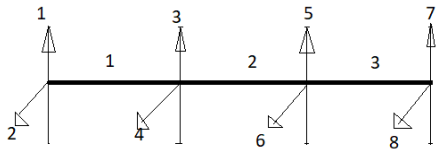

Figure 4.2 A beam with 3 elements/4 nodes and DOF

The assembled stiffness matrix is obtained by summing up DOF at respective nodes where the elements are attached to each other showing a continuity which is given below (8x8):

$$K = \frac{2EI}{L^3}\begin{bmatrix} 6 & 3L & -6 & 3L & 0 & 0 & 0 & 0 \\ 3L & 2L^2 & -3L & L^2 & 0 & 0 & 0 & 0 \\ -6 & -3L & 12 & 0 & -6 & 3L & 0 & 0 \\ 3L & L^2 & 0 & 4L^2 & -3L & L^2 & 0 & 0 \\ 0 & 0 & -6 & -3L & 12 & 0 & 0-6 & 03L \\ 0 & 0 & 3L & L^2 & 0 & 4L^2 & -3L & L^2 \\ 0 & 0 & 0 & 0 & -6 & -3L & 6 & -3L \\ 0 & 0 & 0 & 0 & 3L & L^2 & -3L & 2L^2 \end{bmatrix} \quad [4.4]$$

The assembled mass matrix is given by (8x8):

$$M = \frac{\rho AL}{420}\begin{bmatrix} 156 & 22L & 54 & -13L & 0 & 0 & 0 & 0 \\ 22L & 4L^2 & 13L & -3L^2 & 0 & 0 & 0 & 0 \\ 54 & 13L & 312 & 0 & 54 & -13L & 0 & 0 \\ -13L & -3L^2 & 0 & 8L^2 & 13L & -3L^2 & 0 & 0 \\ 0 & 0 & 54 & 13L & 312 & 0 & 54 & -13L \\ 0 & 0 & -13L & -3L^2 & 0 & 8L^2 & 13L & -3L^2 \\ 0 & 0 & 0 & 0 & 54 & 13L & 156 & -22L \\ 0 & 0 & 0 & 0 & -13L & -3L^2 & -22L & 4L^2 \end{bmatrix} \quad [4.5]$$

4.1.1 Boundary conditions of nanocantilever:

For a cantilever beam, since one end is clamped, and the other is free, motion is constrained at the clamped end and therefore, DOF at the clamped end are eliminated as shown in the *Figure 4.3*:

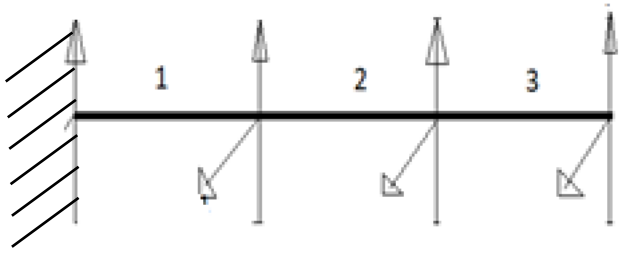

Figure 4.3 A cantilever beam with eliminated DOF at the clamped end

4.1.2 Eigenvalues (ω_r^2) and Eigenvectors (ψ_r) of cantilever beam:

The Eigenvalue equation is written as: $(K - M\omega_r^2)\varphi_r = 0$, where, ω_r^2 represents the Eigenvalues and φ_r represents the Eigenmodes.

Eigenvalues represent the square of natural frequencies and eigenvectors represent the corresponding mode shapes. Angular frequency, ω_r is given in rad/sec and the frequency,

$$f_r = \frac{\omega_r}{2\pi} \text{ (in hertz)}$$

Eigenvalue matrix has a unique value, whereas the multiples of eigenvector matrix represent the same mode shape but with different amplitudes, i.e.,

$$\begin{bmatrix}1\\3\\2\end{bmatrix} \text{ is the same as } \begin{bmatrix}3\\9\\6\end{bmatrix}$$

To account for this indeterminate scaling factor, modal mass and modal stiffness are considered which are shown in the following section.

4.1.3 Modal Mass (m_r) and Modal Stiffness (k_r):

Modal model has orthogonal properties stated as:

$$[\psi]^T[M][\psi] = [m_r]$$
$$[\psi]^T[K][\psi] = [k_r]$$

ψ is the mode shape vector (eigenvector). m_r & k_r are referred to as modal mass and modal stiffness respectively. These values are not unique as they are directly related to eigenvector matrix which is subjected to scaling factor. However, the ratio, $\frac{k_r}{m_r}$ is unique and is equal to its eigenvalue, ω_r^2; i.e.,

$$\omega_r^2 = \frac{k_r}{m_r} \quad [4.6]$$

Natural frequency, *f* in hertz, is given by the equation:

$$f = \frac{1}{2\pi}\sqrt{\frac{k_r}{m_r}} \quad [4.7]$$

4.1.4 Mass-normalised mode shape for mode *r* ($\emptyset_r$):

Modal mass is used to convert the original eigenvector (ψ) to mass-normalized eigenvector ($\emptyset_r$) for mode *r* which has a unique value. Mass-normalized eigenvector, $\emptyset_r$ is given by:

$$\emptyset_r = \frac{[\psi]}{\sqrt{m_r}} \quad [4.8]$$

ψ_r has no units, i.e., dimensionless; while $\emptyset_r$ has units of mass$^{-1/2}$. This value is used in the frequency response function to analyse the response of the system for given excitation conditions. Now that the eigenvalues and eigenvectors of an undamped model are determined, we add damping and see how it affects the frequency and amplitude of the NR.

4.2 Damping:

Damping is a process of energy dissipation that is stored in oscillations. It influences the number of oscillations, as well as the vibration amplitude of the resonator. Dissipation can be due to several causes like clamping loss, thermoelastic loss [58], and gas friction [48]. Damping is classified into structural and viscous damping as shown in the *Figure 4.4*.

For the nanocantilever in our case, it is placed in a vacuum chamber where there is no viscous damping. Therefore, in these NRs, energy is dissipated only due to structural damping. However, these nanocantilevers are single NWs with no connections between them, which shows that damping is only caused due to internal material which is dependent on the stiffness of the material.

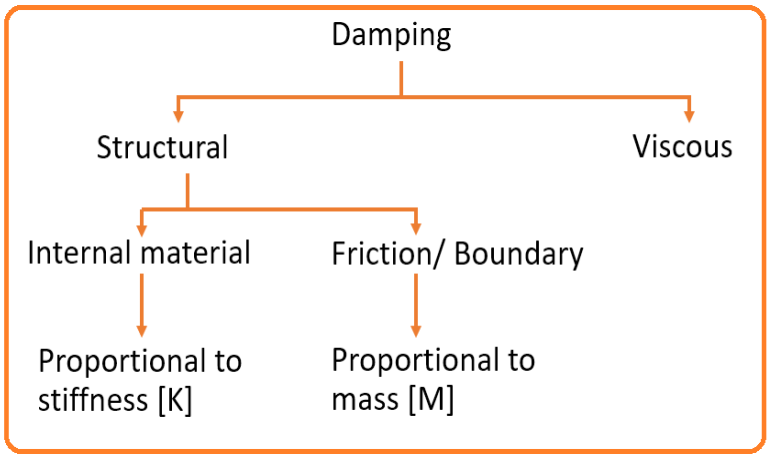

Figure 4.4 Classification of damping

However, as shown in *Figure 4.4*, damping proportional to stiffness or mass matrices is only used for theoretical analysis, but not for real structures. Mode shapes and natural frequencies of proportional damping models are identical to those of the undamped models. This is generally not applied to real structures, as proportional damping overestimates the damping forces and underestimates the vibration amplitudes of the structures.

4.2.1 Internal damping:

Internal damping due to structural material is caused by microstructural defects, dislocations in metals, crystal grain slip, chain movements in polymers, eddy currents. It could also be caused by the hysteresis loop that represents the energy dissipated by unit volume of material per stress cycle.

4.2.2 Thermoelastic damping

When a cantilever is flexurally vibrating, the surface in tension is cooler than the opposite surface in compression, resulting in a heat flow and we must account for thermoelastic damping as a non-recoverable loss of energy [9].

4.2.3 Gas friction damping

This is defined as the dissipation of energy in a material due to fluid friction [58]. Quality factor (explained in Section 4.3) of Si nanocantilevers is high, in the range of 10^3 to 10^4 in high vacuum and starts to decrease when going to higher pressures [48]. However, as we are interested in sharp resonance peaks for high mass sensitivity of cantilevers, it is important to see the effects of damping.

4.3 Measurement of damping:

Damping can be represented using various terms like damping ratio, loss factor, and quality factor/amplification factor. Viscous damping is generally represented using the damping ratio. This is a material-dependent property that can be calculated from experiments. Damping ratio is given by:

$$\zeta = \frac{C}{C_0} = \frac{C}{2\sqrt{KM}} \qquad [4.9]$$

However, in structural damping, damping ratio, ζ is replaced by loss factor, η at resonance. the relation between them can be approximated as:

$$\eta = 2\zeta \quad [4.10]$$

Another measure of damping is the 'Amplification factor' or 'Quality factor'. This is the reciprocal of loss factor and is defined by material properties alone as:

$$Q = \frac{1}{2\zeta} = \frac{\sqrt{MK}}{C} \quad [4.11]$$

Damping ratio is presented as a fraction and describes systems in one of four states:

i. ***Undamped:*** If $\zeta = 0$, it is referred to an undamped model. The system vibrates without any decay in its vibration amplitude.
ii. ***Underdamped:*** The system vibrates with its amplitude exponentially decreasing to zero. If $0 < \zeta < 1$, it is referred to an underdamped model.
iii. ***Critically damped***: This damping is just sufficient to prevent oscillations. If $\zeta = 1$, it lies between underdamped and overdamped conditions and referred as critically damped model.
iv. ***Overdamped:*** Here the system returns to equilibrium without any oscillations. If $\zeta > 1$, it is referred to overdamped model.

For continuous forced NR oscillations to occur, it has to be in the underdamped state. Therefore, simulations on damping of the nanowire would consider values in the range of $0 < \zeta < 1$.

4.4 Calculation of damping matrix

Equation of motion for a structurally damped MDOF system, with N degrees of freedom, is given by:

$$[M]\{\ddot{x}(t)\} + i[D]\{x(t)\} + [K]\{x(t)\} = \{f(t)\} \quad [4.12]$$

The only unknown value in the equation above is the damping matrix, [D]. A simple general way of calculating the damping matrix is 'proportional damping'. This matrix is a linear combination of mass and stiffness matrices given as

$$D = \beta[K] + \Upsilon[M] \quad [4.13]$$

The loss factor (η) of the material is a measure of damping [59] which is independent of the geometrical parameters of the structure and just depends on the material. η_r is the structural damping loss factor for mode *r* for any selected vibrational frequency, ω_r, and is related to β & Υ as:

$$\eta_r = \beta + \frac{\Upsilon}{\bar{\omega}_r^2} \quad [4.141]$$

For **damping proportional to mass** only, $\beta = 0$ and the damping ratio becomes:

$$\eta_r = \frac{\Upsilon}{\bar{\omega}_r^2} \quad [4.15]$$

For **damping proportional to stiffness** only, $\Upsilon = 0$ and the damping ratio becomes:

$$\eta_r = \beta \quad [4.16]$$

$\bar{\omega}_r^2$ is the natural frequency of the undamped system and is given by:

$$\bar{\omega}_r^2 = \frac{k_r}{m_r} \quad [4.17]$$

The r[th] eigen value of the damped system is given by:

$$\lambda_r^2 = \bar{\omega}_r^2(1 + i\eta_r) \quad [4.18]$$

As discussed under the Section 4.2. that the damping in NRs dealt in this thesis depend only the stiffness matrix, *Equation (4.16)* is used in calculating the loss factor which is used to determine the damping ratio from *Equation (4.10)*. Since the NR is in underdamped stage, $0 < \zeta < 1$ is considered to generate a frequency response function explained in Section 4.5.

4.5 Frequency response function (FRF) analysis

Frequency response functions are generated to analyze how the system responds under given harmonic excitation conditions, i.e., the vibration frequency and amplitude of the system.

Displacement (x(t)) and force vectors (f(t)) which are functions of space and time can be written as:

$$x(t) = Xe^{i\omega t} \quad [4.19]$$

$$f(t) = Fe^{i\omega t} \quad [4.20]$$

The general equation of motion for damped MDOF system becomes:

$$([K] + i[D] - \omega^2[M])Xe^{i\omega t} = Fe^{i\omega t} \quad [4.21]$$

$$\alpha(\omega) = \frac{X}{F} = ([K] + i[D] - \omega^2[M])^{-1} \quad [4.22]$$

α(ω) is the FRF parameter and is called 'Receptance.' This is given by the ratio of amplitude and the force.

For any DOF, j,k, and for any mode, r from 1 to N:

$$\alpha_{jk}(\omega) = \sum_{r=1}^{N} \frac{\varphi_{jr}\varphi_{kr}}{(k_r - \omega^2 m_r) + i(\eta_r k_r)} \quad [4.23]$$

The above equation can be mass-normalized and written as:

$$\alpha_{jk}(\omega) = \sum_{r=1}^{N} \frac{\emptyset_{jr}\emptyset_{kr}}{\omega_r^2 - \omega^2 + i(\eta_r \omega_r^2)} \quad [4.24]$$

By plotting a curve using *Equation (4.24),* frequency and amplitude of the nanocantilever can be determined. Verification of Amplitude is discussed in the Section 4.6.

4.6 Verification of values for amplitude

FRF's are generated for a unit force on the beam. For a 1N static force acting on the tip of the beam, i.e., $= 1e^{i\omega t}$ & $\omega = 0$, the deflection, X is given by:

$$\mathrm{X} = \frac{L^3}{3EI} \quad [4.25]$$

4.7 Simulation results and discussion

The aforementioned expressions are implemented on MATLAB (code shown in Appendix D). In Chapter 3, the temperature profile is generated for 0 to 2.6mW of laser power absorbed by the NW.

In the results below, first, the variation in Young's modulus with respect to temperature is plotted to get the best fit curve equations for each of those temperature profiles generated. With this, distributed Young's modulus in a NW for varying laser powers is determined. This is then used to calculate the change in resonance of the nanocantilever due to laser heating.

Second, loss factors η are assumed based on the underdamped condition where damping factor ζ should be in the range of $0 < \zeta < 1$, i.e., $0 < \eta < 2$. This is used to generate FRFs of NWs with both constant and distributed Young's modulus. This focuses on the change in vibration amplitude of the NW due to damping.

Finally, comparison of initial stiffer NWs with the laser heated softer NWs in terms of resonance frequency and amplitude is shown.

4.7.1 Variation in Young's modulus of the nanowire due to its temperature distribution

Young's modulus impacts the stiffness of the beam. Variation in Young's modulus with respect to temperature is an important factor to be considered to calculate change in resonance of the beam due to laser heating. Young's modulus values are taken from literature [60] for a range of temperatures between room and melting point. These values are used to plot variation of Young's modulus in the temperature range of our interest for various laser power fractions. This is then used to find a best fit equation for Young's modulus as a function of length of the NR.

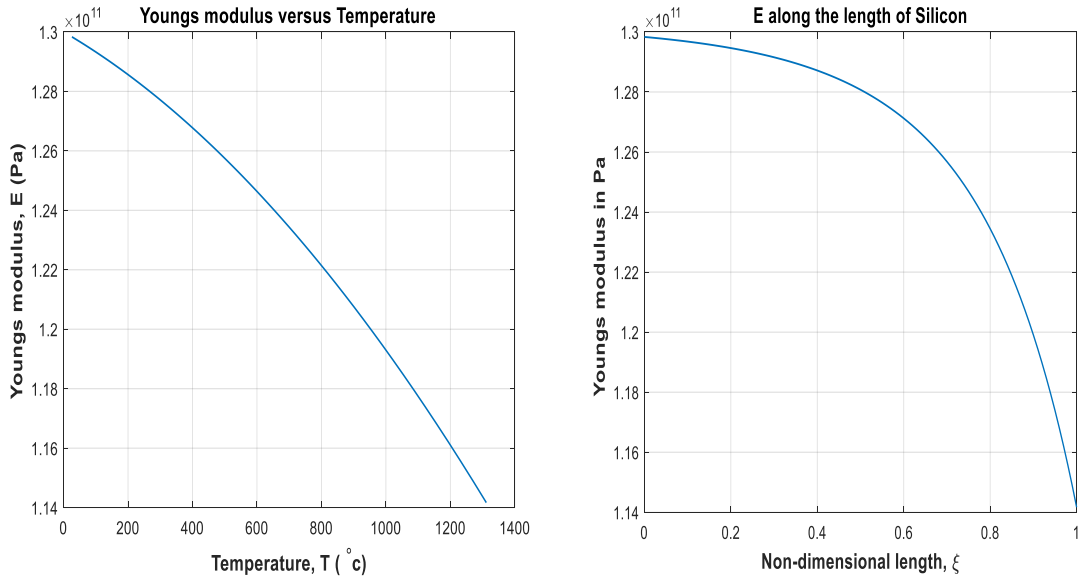

Figure 4.5 (a) Variation of* Young's *modulus with temperature; (b)* Young's *modulus, E (in Pa) along the non-dimensional length (ξ) of SiNW

Figure 4.5(a) shows the variation of Young's modulus as a function of temperature for 1.6 mW of laser power absorbed by the SiNW with a temperature difference of 819 K. *Figure 4.5(b)* shows the variation of Young's modulus as a function of non-dimensional length, ξ for conditions similar to those mentioned in *Figure 4.5(a)*.

The best fit curve equation for Young's modulus, *E*, for 1.6 mW of laser power absorbed by the silicon NW along the non-dimensional length, ξ, is given by:

$$E = -7.8e + 09\xi^4 + 6.1e9\xi^3 - 5.3e^9\xi^2 - 1.2e^9\xi + 1.3e^{11} \quad [4.26]$$

4.7.2 Comparison of numerically calculated resonance with constant Young's modulus and a distributed Young's modulus

Eigenvalues for both NW with constant *E* and NW with distributed *E* are calculated using *Equation (4.7).* These are plotted for varying values of D/L^2 to validate the results of calculated resonances. The generated profile is expected to be linear as the frequency equation of cantilever beams from Euler-Bernoulli derivation is expressed as [63]:

$$f = \frac{\beta_n^2}{8\pi}\sqrt{\frac{E}{\rho}}\frac{D}{L^2} \quad [4.27]$$

Where, f is the frequency, ρ is the density, D is the diameter and L is the length of the NW. β_n is the eigenvalue coefficient derived from the characteristic cantilever equation: $cosh(\beta_n)cos(\beta_n) + 1 = 0$. It is seen from the equation that frequency should be linearly increasing with the ratio D/L^2.

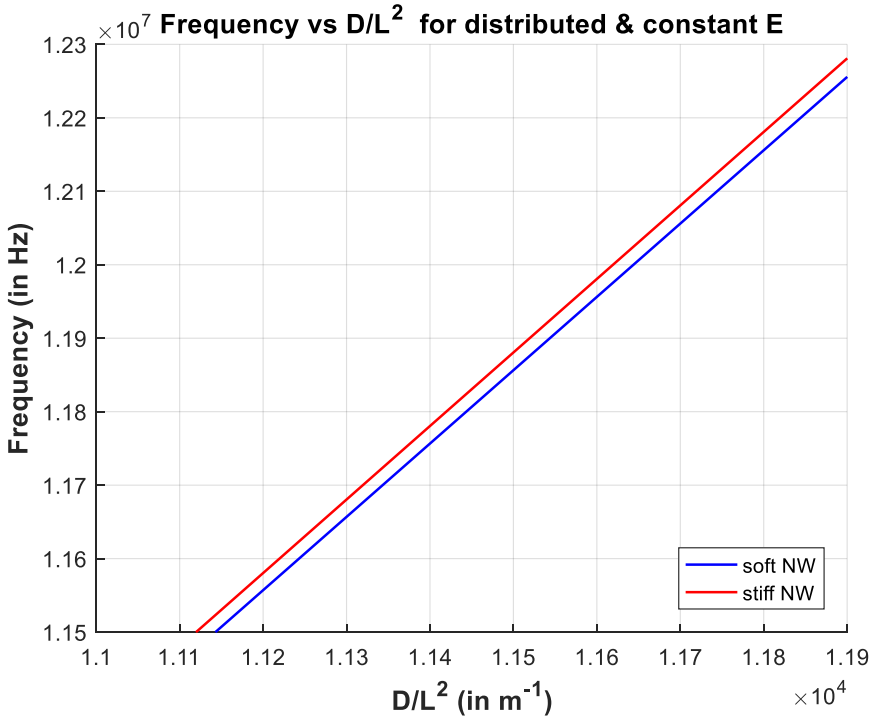

Figure 4.6 Variation of frequency with D/L^2 for stiffer (unheated NW with constant E) and softer (heated NW with distributed E) nanowires

Figure 4.6 is the plot describing how the frequency varies with D/L^2 for a stiffer nanowire (in red) compared to softer NW (in blue). This is plotted as a part of validating the results to show that frequency is linearly increasing with D/L^2 ratio for both the nanowires. It can also be shown that the frequency of a softer NW is less than that of a stiffer NW.

4.7.3 Calculation of resonance shift caused due to laser power

Figure 4.7 clearly shows a frequency downshift with increasing laser heating (softening) of the NW. In this section, temperature profiles for various fractions of laser power absorbed are first taken from the calculations in Section 3.2.1. Then the variation in *E* of these NWs are calculated as shown in Section 4.7.1. With these results, the change in frequency of NWs due to laser heating is calculated and plotted against various fractions of laser power. Based on the data available for the temperature dependence of *E*, laser power absorbed in the range of 0 mW to 2 mW is considered. However, the exact amount of light absorbed by the nanowire during measurements is unknown and depends on the optical properties of the material and wavelength of laser.

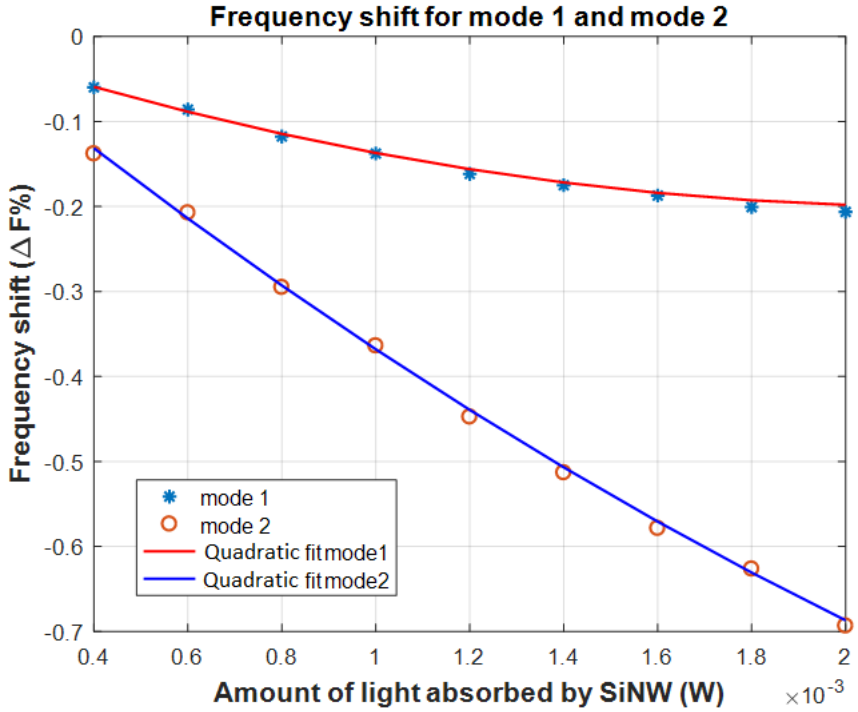

Figure 4.7 Shift in Resonance frequency with amount of light absorbed by the SiNW

From the *Figure 4.7*, it is seen that there is 0.22% of frequency shift (1st mode) for 2mW of laser power absorbed, that is when the temperature difference will be approximately 1069 K. This shift is mode dependent and increases with higher harmonics.

$$\Delta F\% = \left(\frac{F_{DE} - F_{CE}}{F_{CE}}\right) * 100 \qquad [4.28]$$

Where, ΔF is the shift in frequency, F_{DE} is the numerically calculated frequency with distributed Young's modulus and F_{CE} is the frequency with constant Young's modulus.

4.7.4 FRF for a constant Young's modulus, *E*, having a constant loss factor, η:

As discussed in previous chapters, the mass attached to the resonator will lower the resonance frequency of the NR. However, the frequency shift depends not only on the attached mass, but also on the position of attached particles and the vibration amplitude of the resonator [34]. Therefore, it is important to accurately know the position of the particle and amplitude of the resonator.

Also, during the frequency measurements, if the vibration amplitude of the resonator is

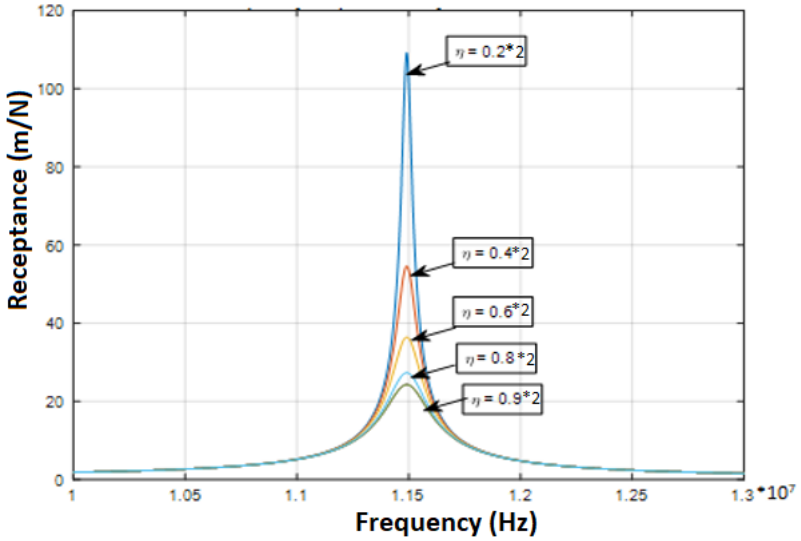

Figure 4.8 FRF of a NW at room temperature with different values of constant loss factor

too small, the resonance peak cannot be detected. In this section, we show how the frequency and amplitude change with the increase of damping.

The loss factor is varied from (0.2% to 0.9%) *2 (for the underdamped case) and the variation of amplitude is seen. Loss factor value less than 0.2% *2 is not shown in the plot (*Figure 4.8*) due to large variation in amplitude (which cannot be captured properly in the graph). The relation of the amplitude to the loss factor is seen in *Figure 4.9*, in which we see that the reduction in amplitude decreases with increase in loss factor.

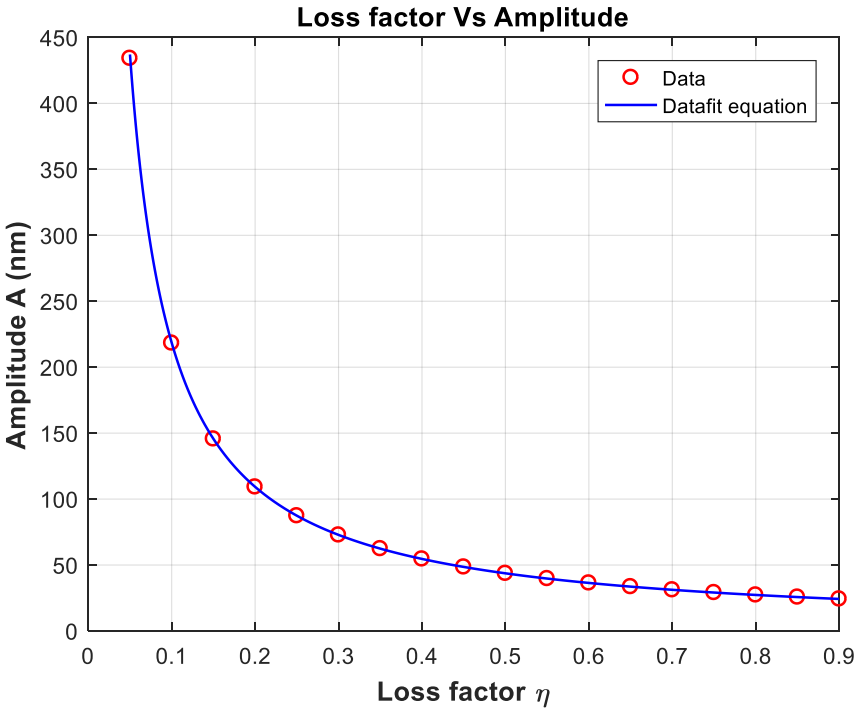

Figure 4.9 Variation of amplitude with increase in loss factor (Q^{-1}).

Amplitude *A* decreases with increase in loss factor η, with a steeper curve in the beginning than at the end. A power-law with exponent -1 provides an excellent fit, as seen in Figure 4.9. The curve is thus seen to be the hyperbola:

$$A = 21.86/\eta \qquad [4.29]$$

For force measured in nano-Newtons, amplitude is measured in nanometres, as shown.

4.7.5 FRF for a distributed Young's modulus, *E*, and distributed loss factor, *η*:

It is reported in the literature that the quality factor (Q) of silicon resonators decreases with increase in temperature [56], [61]. Therefore, the loss factor which is inversely proportional to Q (shown in *Equation (4.11)*) increases with increase in temperature of the NW. A laser-heated nanowire will have a distributed Young's modulus as well as a distributed loss factor. Since the exact value of loss factor is unknown, a variation in loss factor according to variation in temperature of the laser heated NW is considered.

Figure 4.10, values of loss factor η for the laser heated NW are higher than for the unheated NW, and have a temperature-dependent distribution along the NW; i.e. if a NW of constant E has a η value of 0.2% *2, then the NW of varying E may have a η value of (0.2 to 0.3 %) *2. We observe from the graph that the amplitude decreases for higher average loss factor. Despite the fact that the graph looks similar to the *Figure 4.9*, we note that the resonance frequency is shifted from its natural frequency by kHz due to laser heating.

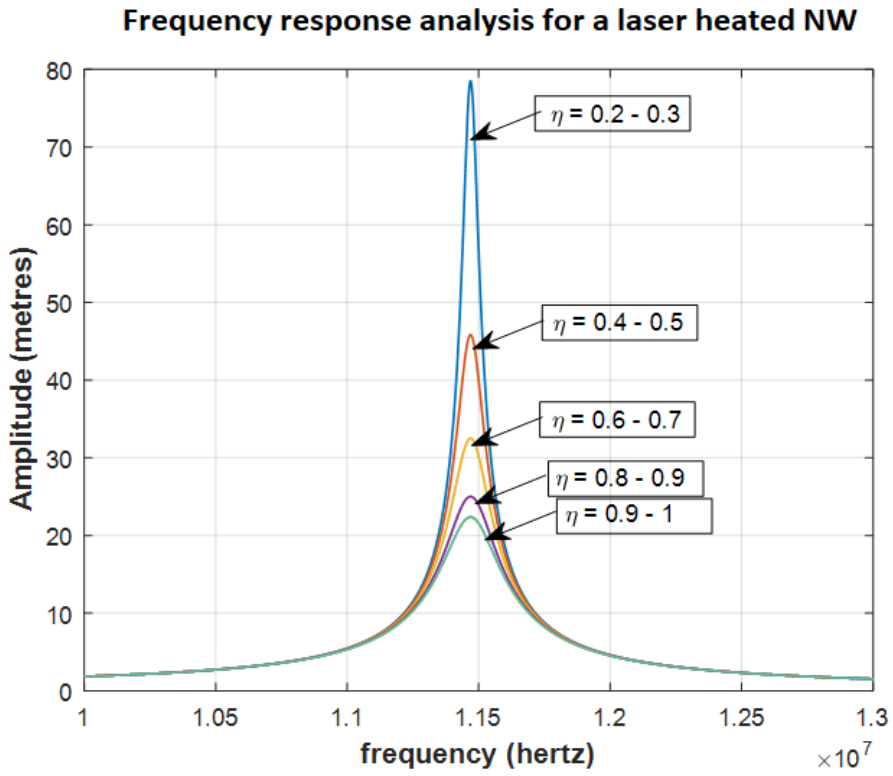

Figure 4.10 FRF of NW with varying E and a distributed loss factor

Measurement of internal material damping is crucial in studying the dynamic properties of a structure. This analysis can be used during nanoresonator design, to decide on the minimum gap between the substrate and the NR. This can also potentially serve as a method to determine material damping in resonators due to variation in temperatures, for a known value of resonant amplitude from experiments.

4.7.6 Comparison of FRF for a distributed Young's modulus, *E*, with both constant and a distributed loss factor, *η*

What would be the difference if a constant loss factor (η) is considered instead of a distributed η? In this section, variation of amplitude in terms of both constant loss factor and a distributed loss factor for a heated nanowire whose stiffness is varying along its length is seen in the *Figure 4.11*

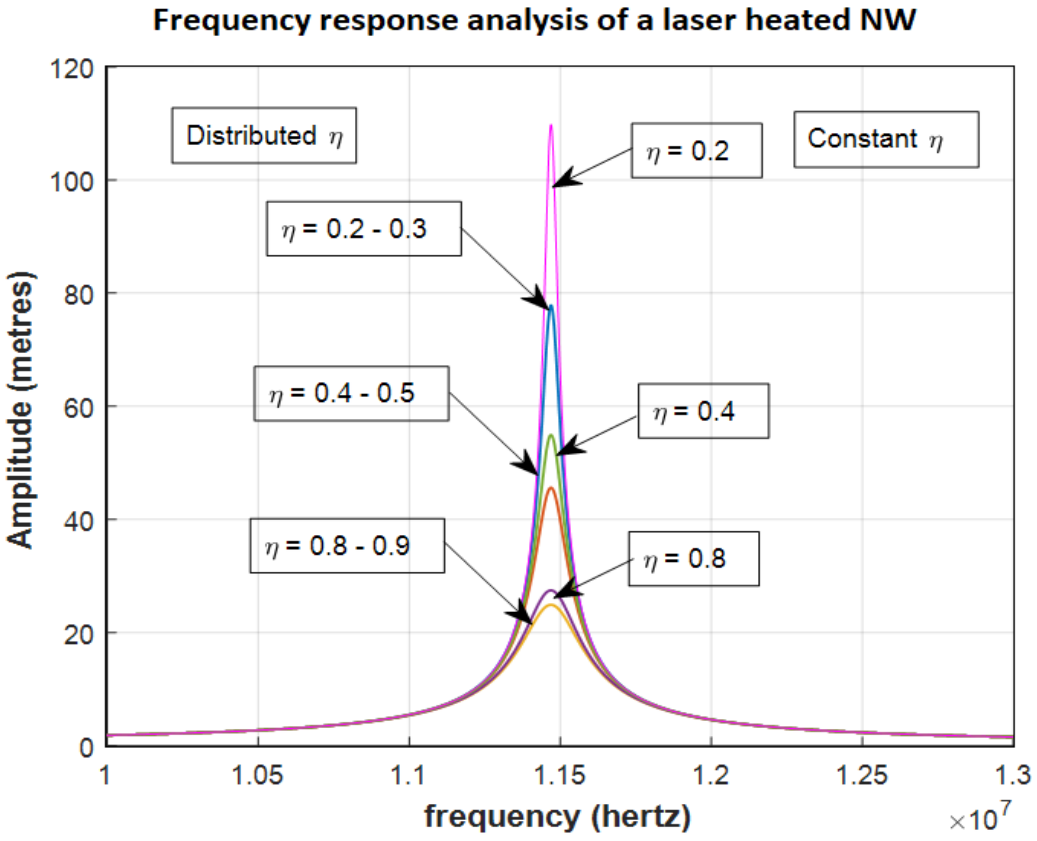

Figure 4.11 FRF showing the difference between a constant and varying loss factors for nanowire with distributed* Young's *modulus

4.7.7 Comparison of FRF of a stiffer nanowire with a softer nanowire:

In *Figure 4.12*, a NW at room temperature with constant Young's modulus and damping coefficient, is compared with a heated nanowire whose stiffness and damping coefficient is varying along its length.

We see that the softer nanowire has a lower resonance frequency and a reduction in amplitude due to increased damping with increase in temperature.

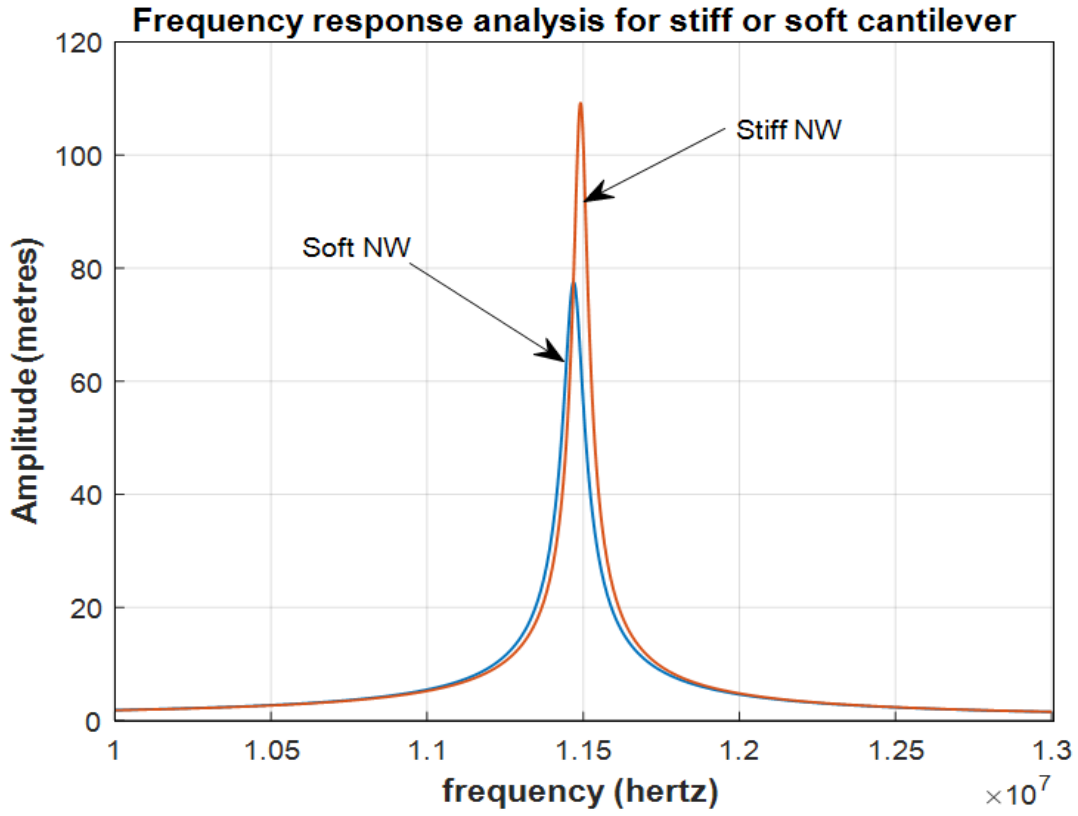

Figure 4.12 Comparison of stiffer NW with Softer NW

One might argue that the amplitude of a softer wire is always higher than the stiffer wire. It is certainly true that as the stiffness of the structure decreases, the amplitude increases. However, we are not considering two NWs with a large difference in the *E* value. *E* of laser heated NW varies along the length of it, however, it is still the same at the clamped end. *Figure 4.13* shows how the amplitude varies for NWs with different values of *E*. In the *Figure 4.12*, amplitude of the relatively soft nanowire due to laser heating is less than the unheated nanowire because of the effect of internal damping.

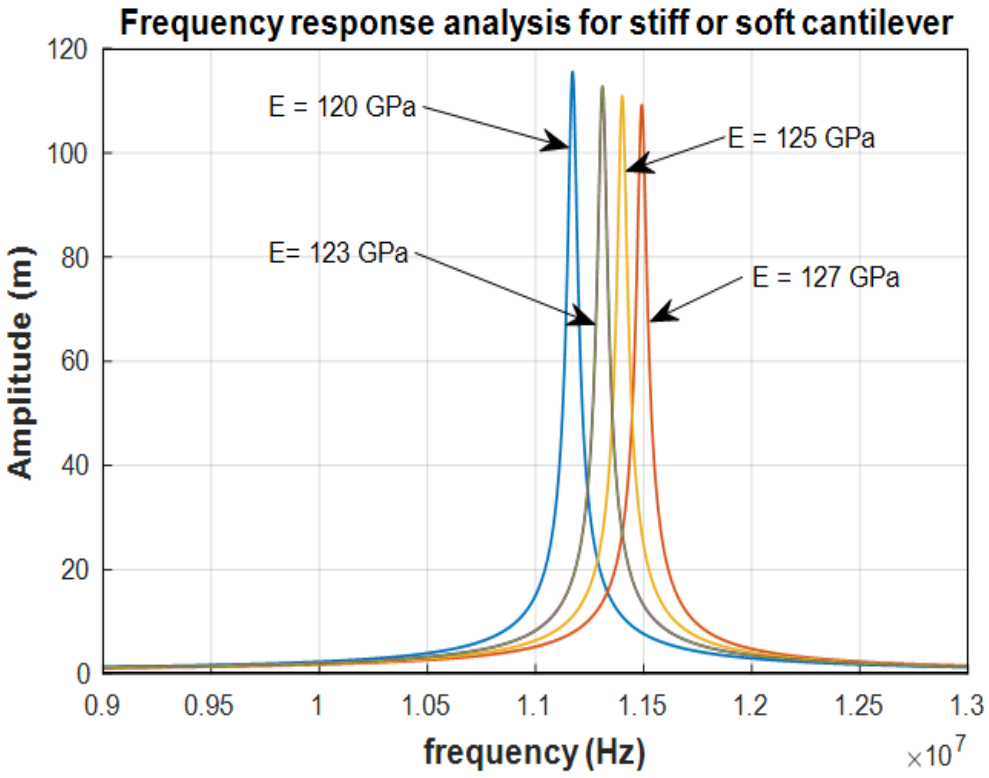

Figure 4.13 Change in amplitude of NWs with different* Young's *modulus E

This is to show that the variation in frequency and amplitude will be due to both stiffness and damping of the NR.

Chapter 5: Euler-Bernoulli Derivation for a beam of varying Young's Modulus and a mass added at the tip

As discussed in previous chapters, absorption of laser power produces a temperature distribution inside the NW. This causes the Young's modulus to vary along the length of the NW. Euler-Bernoulli framework gives an analytical beam equation to calculate the frequency of a beam with uniform Young's modulus. However, as shown in Chapter 4, modal analysis based on discretizing the beam into elements is the only method to calculate frequencies of a beam with non-uniform Young's modulus. So, in this chapter, a method using a ***Semi-analytical Equation*** is derived to enable calculation of frequencies of a beam with empirical information on the variation of Young's modulus.

The method derived is compared, initially, with three other methods which are: ***Modal analysis*** (*Equation 4.1* in chapter 4), ***Euler-Bernoulli Equation (E-B)*** (*Equation 5.38*), and the ***Blevins fundamental frequency equation*** [62] (*Equation5.41*). We show that the Semi-analytical method derived in this chapter is the most accurate among these methods.

Second, this derivation is extended to calculate the frequency of a beam with a mass attached at its tip. This is shown to be a reliable method to calculate the frequency shift of a heated NR (varying *E*) due to an attached mass**.** A single-degree-of freedom (**1DOF**) model **(***Equation 5.43*) which is the simplest and most frequently used model in literature, implicitly assumes the mass to be uniformly distributed along the length of the beam. The Semi-analytical Method is compared with each of the three other methods as well as with the **1DOF *equation*** for calculating the attached mass based on frequency shift. This quantifies why Semi-analytical method should be used instead of other methods for accurate mass measurements.

5.1 Derivation of general form of theoretical resonance frequency

Consider the transverse vibrations of a beam in the x-y plane as shown in the *Figure (5.1)* of length *L*, which is subjected to transverse loading. The general equation of motion for transverse vibrations of a beam is given by [63]:

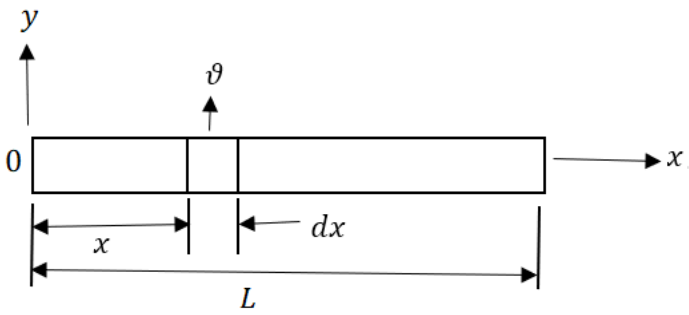

Figure 5.1 Transverse vibrations of a beam in the x-y plane

$$\frac{\partial^2}{\partial x^2}\left[E(x)I(x)\frac{\partial^2 \vartheta}{\partial x^2}\right]dx + m(x)dx\frac{\partial^2 \vartheta}{\partial t^2} = f(x,t) \quad [5.1]$$

E is the Young's modulus of the beam, I is moment of inertia, and product $E(x)I(x)$ gives the flexural rigidity of the beam. ϑ is the deflection and f being the force acting on the beam along the x direction in time t. $m(x) = \rho(x)A(x)$ represents the mass per unit length of the beam which is equal to the density times cross-sectional area of the beam.

For free vibrations, the force, $f(x,t) = 0$ and the deflection, which is a function of space and time can be written as [63]:

$$\vartheta(x,t) = X(x)e^{i\omega t} \quad [5.2]$$

where, ω is the angular frequency in radians/second and X(x) is the mode shape. By substituting this in the Eq. (5.1), we can write:

$$\frac{d^2}{dx^2}\left[E(x)I(x)\frac{d^2X}{dx^2}\right] - m(x)\omega^2 X = 0; 0 \le x \le L \quad [5.3]$$

By introducing non-dimensional lengths, ξ, and a parameter k for a later convenience:

$$\xi = \frac{x}{L} \; and \; k = \omega^2 L^4 \quad [5.4]$$

With these parameters, Eq. (5.3) can be written as:

$$\frac{d^2}{d\xi^2}\left[E(\xi)I(\xi)\frac{d^2X}{d\xi^2}\right] - km(\xi)X = 0; 0 \leq \xi \leq 1 \quad [5.5]$$

For a beam of uniform stiffness, this equation becomes:

$$EI\left[\frac{d^4X}{d\xi^4}\right] - km(\xi)X = 0; 0 \leq \xi \leq 1 \quad [5.6]$$

However, for a beam whose temperature is rising due to induced laser power, mechanical properties such as the Young's modulus vary along the beam and hence the equation must be re-written accordingly and is shown in Section 5.2.

Variation in Young's modulus of the Silicon nanocantilever for a laser power of 1.6mW is given by *Equation 4.26.*:

$$E = -7.8e^9\xi^4 + 6.1e^9\xi^3 - 5.3e^9\xi^2 - 1.2e^9\xi + 1.3e^{11}$$

5.2 Derivation of theoretical resonance frequency with varying stiffness

For a beam with a constant moment of inertia and a mass density but with varying Young's modulus, we write the equation as:

$$I\frac{d^2}{d\xi^2}\left[E(\xi)\frac{d^2X}{d\xi^2}\right] - kmX = 0; 0 \leq \xi \leq 1 \quad [5.7]$$

Several researchers have worked on various methods using closed form solution [64], non-uniform power series [65], Fredholm integrals [65], for isotropic beams with varying cross-sections [66], non-uniform beams with varying material density and elastic modulus [64], [65]. This work follows the numerical procedure using Fredholm integrals [65], and is built on it to find the frequency of a beam with varying stiffness and a mass attached at the tip.

The above Eq. (5.7) is integrated 4 times with respect to ξ from $0\ to\ \xi$ using Fredholm integral equations and the resulting equation is written as:

$$\boldsymbol{E(\xi)IX(\xi) + I(s)\int_0^{\xi}\left[E''(s)(\xi - s) - 2E'(s) - \frac{1}{6}km(\xi - s)^3\right]X(s)ds = \frac{c_1}{6}\xi^3 + \frac{c_2}{2}\xi^2 + c_3\xi + c_4} \quad [5.8]$$

To calculate the four constants in the Eq. (5.8), four boundary conditions of the cantilever beam are required which is shown in the following section.

5.2.1 Boundary conditions of the nanocantilever

For a beam clamped at one end, $\xi = 0$, and free at the other end $\xi = 1$, we have, Deflection (X), slope (Θ), Bending Moment (M) and the shear force (Q) as:

$$At\ \xi = 0;\ X = 0\ \&\ \Theta = 0 \quad [5.9]$$

$$At\ \xi = 1;\ M = 0\ \&\ Q = 0 \quad [5.10]$$

Based on the equations (5.9) and (5.10), we can calculate the coefficients c_1, c_2, c_3, and c_4 as:

$$C_1 = -k\int_0^1 m(s)\,X(s)ds \quad [5.11]$$

$$C_2 = -k\int_0^1 (1-s)m(s)\,W(s)ds + k\int_0^1 m(s)\,X(s)ds \quad [5.12]$$

$$C_3 = C_4 = 0 \quad [5.13]$$

By using these conditions in the Eq. (5.8), we get the integral equation:

$$E(\xi)IX(\xi) + \int_0^{\xi} K_1(\xi, s)\,X(s)ds + k\int_0^1 K_2(\xi, s)\,X(s)ds = 0 \quad [5.14]$$

Where K_1 & K_2 are given by:

$$K_1(\xi, s) = IE''(s)(\xi - s) - 2IE'(s) \quad [5.15]$$

$$K_2(\xi, s) = \begin{cases} \frac{1}{6}ms^2(s - 3\xi) & ;0 \le s \le \xi \\ \frac{1}{6}m\xi^2(\xi - 3s) & ;\xi < s \le 1 \end{cases} \quad [5.16]$$

By substituting Equations. (5.15) & (5.16) in the above Eq. (5.12), natural frequencies of the beam can be obtained. However, the mode shapes $X(\xi)$ are unknown and can be obtained by expanding it as power series:

$$X(\xi) = \sum_{N=1}^{n+1} c_N \xi^N \qquad [5.17]$$

Where, c_N are the unknown coefficients with n as a positive number chosen large enough to have a negligible error. By substituting this in the Eq. (5.14), we get:

$$\sum_{N=1}^{n+1} c_N \xi^N E(\xi) I + \sum_{N=1}^{n+1} c_N \int_0^1 K_1(\xi, s)\, s^N ds + k \sum_{N=1}^{n+1} c_N \int_0^1 K_2(\xi, s)\, s^N ds = 0 \qquad [5.18]$$

If this equation is multiplied by ξ^M and integrated with respect to $\xi \; from \; 0 \; to \; 1$, we get,

$$\sum_{N=1}^{n+1} (e_{MN} + K_{1MN} + kK_{2MN}) c_N = 0; where, M = 1,2 \ldots . (n+1) \qquad [5.19]$$

Where,

$$e_{MN} = I \int_0^1 \xi^{M+N} E(\xi) d\xi \qquad [5.20]$$

$$K_{jMN} = \int_0^1 \int_0^1 K_j(\xi, s) \xi^M s^N ds d\xi; \quad j = 1,2 \qquad [5.21]$$

Natural frequencies from *k*, can be obtained by substituting Eqns. (5.20) & (5.21) in Eq. (5.19) and equating the determinant of the co-efficient matrix to 0.

$$\det(e_{MN} + K_{1MN} + kK_{2MN}) = 0 \qquad [5.22]$$

The *k* obtained from this equation is substituted back in the Eq. (5.19) to obtain mode shapes of the beam. With this, frequency of a beam with varying Young's modulus can be determined. In the next section, a mass is attached to the tip of the beam, and the equations are derived to calculate the frequency of it.

5.3 Calculation of resonance with an attached mass

Consider a mass attached at the tip of the sensor, whose frequency is to be calculated. The boundary conditions of the cantilever sensor will be as follows:

5.3.1 Boundary conditions of the nanocantilever with an attached mass

For a beam clamped at one end, $\xi = 0$, and free at the other end $\xi = 1$, we have, Deflection (W), slope (Θ), Bending Moment (M) and the shear force (Q) as:

$$At\ \xi = 0;\ X = 0\ \&\ \Theta = 0 \quad [5.23]$$

$$At\ \xi = 1;\ M = 0\ \ \&\ \ \mathrm{Q} = L^3 m_0 \omega^2 X(\xi) \quad [5.24]$$

Based on the equations (5.23) and (5.24), we can calculate the coefficients C_1, to C_4 of equation (5.8) as:

$$C_1 = L^3 m_0 \omega^2 X(\xi = 1) - k \int_0^1 m(s)\, X(s) ds \quad [5.25]$$

$$C_2 = k \int_0^1 (s) m(s)\, W(s) ds - L^3 m_0 \omega^2 X(\xi = 1) \quad [5.26]$$

$$C_3 = C_4 = 0 \quad [5.27]$$

By using these conditions in the Eq. (5.8), we get the integral equation as:

$$E(\xi) I X(\xi) + \int_0^{\xi} K_1(\xi, s)\, X(s) ds + k \int_0^1 K_2(\xi, s)\, X(s) ds + k K_3(\xi) = 0 \quad [5.28]$$

Where K_1 & K_2 are given by:

$$K_1(\xi, s) = IE''(s)(\xi - s) - 2IE'(s) \quad [5.29]$$

$$K_2(\xi, s) = \begin{cases} \frac{1}{6} m s^2 (s - 3\xi) & ; 0 \le s \le \xi \\ \frac{1}{6} m \xi^2 (\xi - 3s) & ; \xi < s \le 1 \end{cases} \quad [5.30]$$

$$K_3(\xi) = \frac{1}{6L}\xi^2(3-\xi)m_0X \quad [5.31]$$

By substituting the coefficients in the Eq. (5.8), natural frequencies of the beam can be obtained. However, the mode shapes $X(\xi)$ are unknown and can be obtained by expanding it as power series:

$$X(\xi) = \sum_{N=1}^{n+1} c_N\xi^N \quad [5.32]$$

By substituting this in the Eq. (5.28), we get:

$$\sum_{N=1}^{n+1} c_N\xi^N\, E(\xi)I + \sum_{N=1}^{n+1} c_N \int_0^1 K_1(\xi,s)\, s^N ds + k\sum_{N=1}^{n+1} c_N \int_0^1 K_2(\xi,s)\, s^N ds = kc_{N+1}\xi^{N+1}\frac{1}{6L}\xi^2(3-\xi)m_0 \quad [5.33]$$

If this equation is multiplied by ξ^M and integrated with respect to $\xi\ from\ 0\ to\ 1$, we get,

$$\sum_{N=1}^{n+1}(e_{MN} + K_{1MN} + k(K_{2MN} + m_0K_{3MN}))c_N = 0;\ \ M = 1,2\ldots.(n+1) \quad [5.34]$$

Where,

$$e_{MN} = I\int_0^1 \xi^{M+N}E(\xi)d\xi \quad [5.35]$$

$$K_{jMN} = \int_0^1\int_0^1 K_j(\xi,s)\xi^M s^N ds d\xi;\quad j = 1,2 \quad [5.36]$$

$$K_{3M} = \int_0^1 \frac{1}{6L}\xi^2(3-\xi)\,\xi^{M+N}d\xi \quad [5.37]$$

Natural frequencies can be obtained by finding a non-trivial solution for the Eq. (5.34)

5.4 Simulation results and discussion

In this section, Equations from the Semi-analytical method above are implemented in MATLAB (shown in Appendix E) to generate frequencies of beams with both uniform and non-uniform *E*.

5.4.1 Comparison of non-dimensional natural frequencies for a beam of uniform Young's modulus

In this sub-section, results for beams of uniform *E* are considered to which the Euler-Bernoulli equations are applicable. This is done to validate the current results against already proven Euler-Bernoulli equation and modal analysis results. Natural frequencies of a homogenous (uniform Young's modulus) silicon cantilever can be calculated using the Euler-Bernoulli equation [63]:

$$f = \frac{\beta_n^2}{8\pi}\sqrt{\frac{E}{\rho}}\frac{D}{L^2} \qquad [5.38]$$

Table 1: Comparing the non-dimensional natural frequencies, ω_{ND}, of Semi-analytical simulation results against Modal analysis, Euler-Bernoulli and Fundamental frequency Equation for a beam of uniform stiffness

Modes	Semi-analytical simulation	Modal analysis simulation (*Equation 4.1*)	Euler-Bernoulli equation (*Equation 5.38*)	Fundamental frequency Eqn. (*Equation5.41*)
1	3.51601	3.51601	3.51601	3.53553
2	22.0345	22.0345	22.0345	-
3	61.6972	61.6972	61.6972	-
4	120.9020	120.9020	120.9020	-

Non-dimensional natural frequencies of this silicon cantilever with uniform stiffness were calculated for the first four modes using the above equations from Semi-analytical method in this chapter. Semi-analytical method expands the modes shapes using power series with 10^{th} order of polynomial (*Equation 5.32*); Modal analysis simulation was carried out by discretizing the beam into 100 elements. However, lower modes require lower orders of

polynomial or fewer elements for Semi-analytical method, and Modal analysis respectively to get the same accuracy. These results are compared against modal analysis simulation (using equation 4.1), Euler-Bernoulli equation (using equation 5.38), and fundamental frequency Eqn. [62] (*Equation5.41*) and shown in *Table 1*. The non-dimensional natural frequencies (ω_{ND}) are calculated as:

$$\omega_{ND} = \omega L^2 \sqrt{\frac{\rho A_c}{EI}} \qquad [5.39]$$

5.4.2 Relative frequency shift for varying fractions of laser power due to distributed Young's modulus, *E*

As the laser power is absorbed by the nanowire during its resonance measurements, we see a distributed temperature along its length. With these values of temperatures, Young's

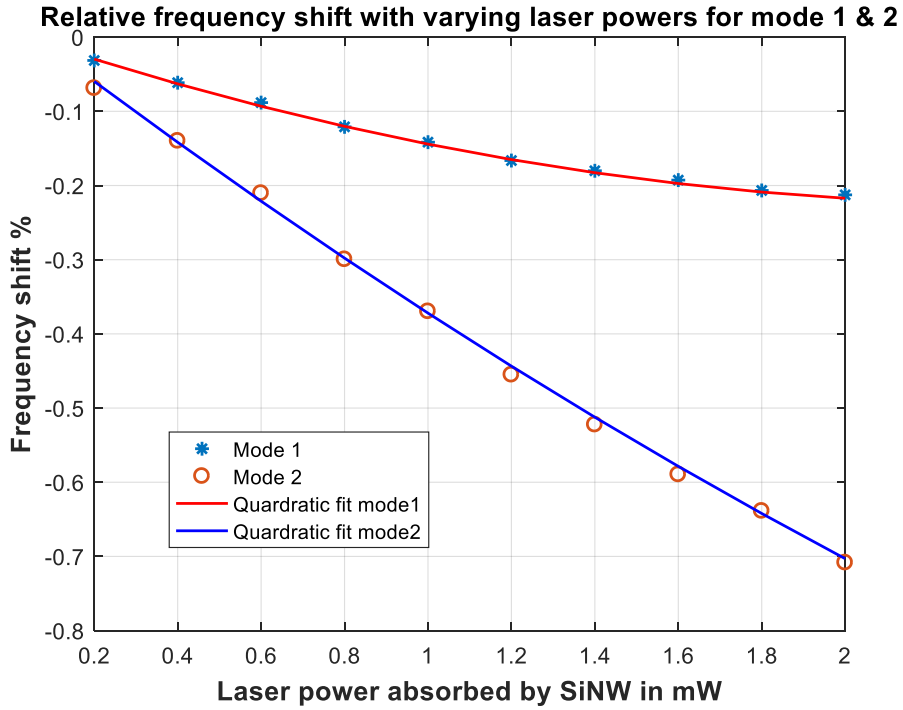

Figure 5.2 Relative frequency shift due to absorption of laser power

modulus *E* is calculated as a function of length for varying fractions of laser power from 0.2 mW to 2 mW and the resonance is calculated accordingly. The effect of laser heating

on the resonance shift of Si cantilever is shown in Section 4.7.3. Here the results are validated by showing resonance shift for the first are second modes due to laser absorption. It is plotted in the *Figure 5.2*.

Relative resonance shift percentage is calculated as:

$$\Delta F\% = \left(\frac{F_{DE} - F_{CE}}{F_{CE}}\right) * 100 \qquad [5.40]$$

5.4.3 Effective stiffness of the laser heated beam

When a SiNW with a uniform Young's modulus *E* of 130 GPa [67] is heated by various fractions of laser power, its stiffness decreases, and the NW will have a distributed Young's modulus along its length, based on which the resonance shifts. However, correction factor can be given by calculating the effective modulus, E_{eff} given in the Table 2 below:

Table 2: Effective Young's modulus *E* value for varying fractions of laser power

Sl. Num	laser power (mW)	Effective *E* for heated SiNW (in Pa)
1	0.2	1.29918E+11
2	0.4	1.29840E+11
3	0.6	1.29771E+11
4	0.8	1.29686E+11
5	1	1.29632E+11
6	1.2	1.29568E+11
7	1.4	1.29532E+11
8	1.6	1.29499E+11
9	1.8	1.29463E+11
10	2	1.29448E+11

To calculate the effective modulus, E_{eff} frequency of a beam with varying *E*, generated using Semi-analytical method is substituted in the Euler-Bernoulli equation (*Equation 5.38*). The temperature difference between the clamped and free tips of the NW at 2mW

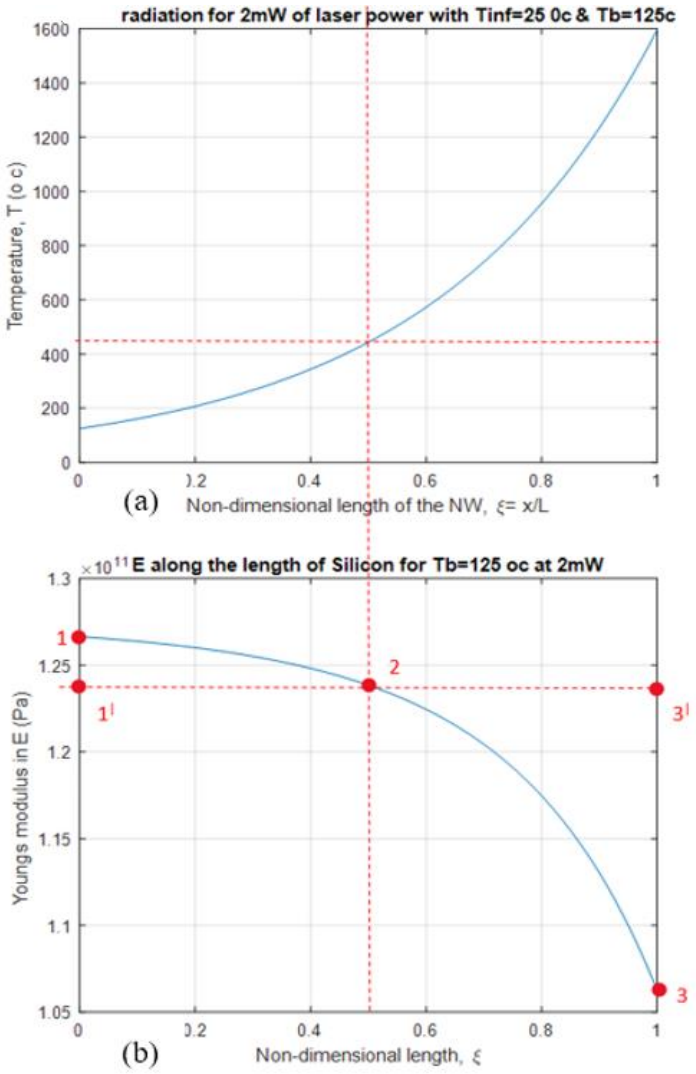

Figure 5.3 For 2mW of laser power absorbed, (a) Variation in temperature of the NW and (b) Variation in *E* of the NW

is 1068K. However, in the Table 2, we see that the deviation in effective *E* is very small from the *E* at room temperature (130 GPa) even for the highest laser power of 2mW. Does a given length of beam near the rigidly clamped end contribute more to the overall stiffness than the same length near the free tip? To answer this question, we considered the stiffness dependence on distance of the NW Section from the clamped end. As shown Table 3 shows calculated frequencies for three test distributions of Young's modulus E(x). A NW with base temperature 100^0C greater than the surrounding temperature and which absorbs

2mW of laser power is considered (*Figure 5.3 (a)*). Variation of *E* along its length is plotted in (*Figure 5.3 (b)*). Columns in Table 3 show frequencies calculated for:

E_1(x): *E(x)* calculated at each NW section, from the temperature distribution. (shown by the curve through points 1-2-3 (*Figure 5.3(b)*).

E_2(x): *E(x)* taken as in E_1, from clamped end to the mid point, and then set to a constant value from mid point of the beam (so as to test the effect of making half of the beam close to the free end have a higher modulus than the true value), shown by the curve 1-2-3' (*Figure 5.3(b)*)

E_3(x): *E(x)* values are made constant along the length of the nanobeam using the value of *E* from the midpoint of the NW (so as to test the effect of make *E* lower for the first half between clamped end and mid point, and higher as in the second case from mid point to free end). shown by the curve 1'-2-3'(*Figure 5.3(b)*)

Table 3: Calculated frequencies (Hz) of NW with assumed modulus distributions E_1(x), E_2(x) and E_3 (x) as described in the text.

S. No.	**Laser power (mW)**	***f*** **(E_1(x))**	***f*** **(E_2(x))**	***f*** **(E_3(x))**
1	0.2	1.14546e+07	1.14548e+07	1.14454e+07
2	0.4	1.14493e+07	1.14497e+07	1.14301e+07
3	0.6	1.14441e+07	1.14447e+07	1.14140e+07
4	0.8	1.14390e+07	1.14399e+07	1.13973e+07
5	1	1.14342e+07	1.14355e+07	1.13806e+07
6	1.2	1.14300e+07	1.14317e+07	1.13649e+07
7	1.4	1.14266e+07	1.14289e+07	1.13513e+07
8	1.6	1.14244e+07	1.14271e+07	1.13409e+07
9	1.8	1.14234e+07	1.14265e+07	1.13345e+07
10	2	1.14236e+07	1.14271e+07	1.13324e+07

Comparing values for 2 mW (last row, #10 in Table 3), the effect of artificially increasing the modulus for the unclamped half of the beam (Case E_2) is overshadowed by the effect of artificially decreasing the modulus for the clamped half. This shows that the change in

overall stiffness (frequency) is dominated by stiffness at the clamped end rather than the free end.

5.4.4 Resonance shift due to attached mass at tip of the cantilever

A cantilever with different masses (Δm) of 0, 3e-18 Kg and 3e-17 kg attached at its tip is considered and below is the image (*Figure 5.4*) showing how the resonance downshifts with the mass attached at the tip of the cantilever. However, a decrease in amplitude is also observed with an addition of mass.

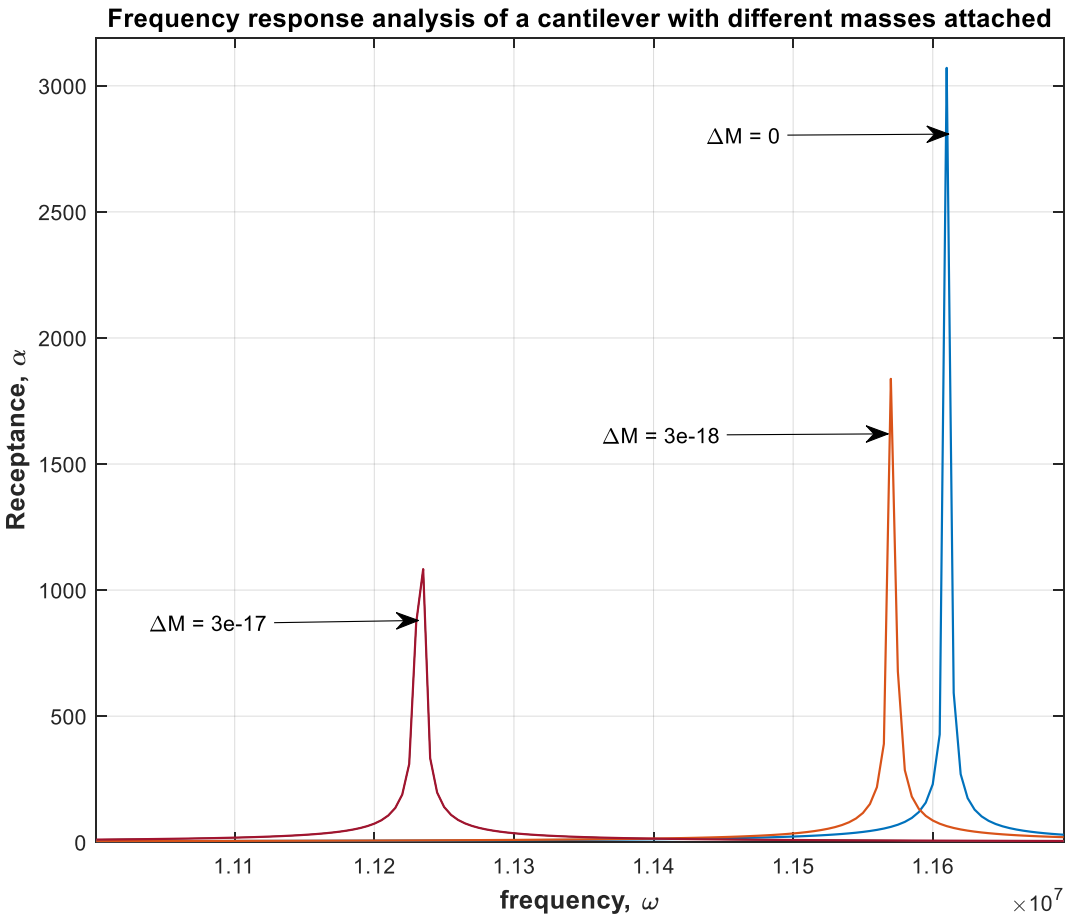

Figure 5.4 Resonance shift due to attached mass at the tip of the cantilever

Frequency downshifts with an addition of a mass as shown in the *Figure 5.4*. However, this value does not match with the frequency shift calculated using the 1DOF equation (*Equation 5.43*), which will be discussed in the Section 5.4.6.

5.4.5 Resonance shift due to mass attached at different locations of the cantilever

Resonance shift for a mass attached at different locations compared to a beam with no mass attached is seen in the picture below (*Figure 5.5*). We observe that the frequency shift is larger when the mass is attached close to the tip and decreases as it is attached away from the tip.

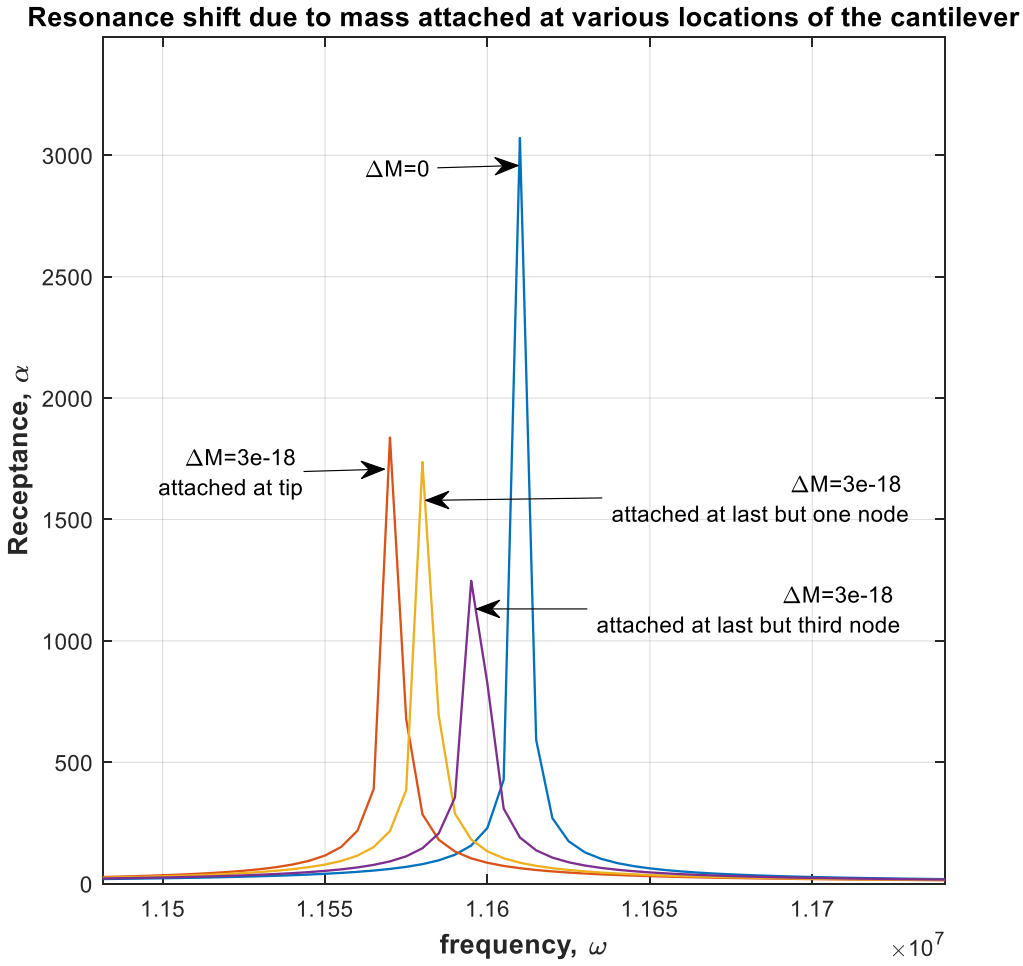

Figure 5.5 Resonance shift due to mass attached at different locations of the cantilever

Using the 1DOF equation is equivalent to assuming that the mass is uniformly distributed along the length of the NR. Considering the position of the mass attached can give accurate calculations.

5.4.6 Comparison of frequency shift between Euler-Bernoulli, Semi-analytical, and the modal analysis models

Resonance frequency of a beam with a mass attached at the tip is compared for four methods listed below:

1. An equation for the fundamental frequency of uniform beams with concentrated masses at the tip is given by [47]:

$$f = \frac{1}{2\pi}\left[\frac{3EI}{L^3(m + 0.24m_0}\right]^{1/2} \quad [5.41]$$

2. Semi-analytical method is the method derived in this chapter.
3. The equation solved using modal analysis is given by

$$f = \frac{1}{2\pi}\left[\frac{K}{m}\right]^{1/2} \quad [5.42]$$

where, *K* is the stiffness of the beam.

4. A general expression relating frequency shift to added mass is obtained by taking the derivative of Eq. (5.42) and is given by:

$$\frac{\Delta \mathrm{f}}{f} = -\frac{1}{2}\frac{\Delta m}{m} \quad [5.43]$$

This 1 DOF expression considers the mass to be uniformly distributed along the cross-Section of the beam.

Resonant frequencies of a beam with a mass of 3E-18 Kg attached at the tip are compared against 4 methods shown in Table 4, for three modes.. Resonance shift is given by the difference between the frequency of a beam with no mass attached and a beam with a mass attached.

$$\Delta f = f_1 - f_2 \quad [5.44]$$

f_1 - frequency of a beam with no mass attached

f_2 - frequency of a beam with a mass of 3E-18 (Kg) attached at the tip of the cantilever

Table 4: Resonance frequency of a beam with a mass of 3E-18 Kg attached at the tip of the cantilever

Methods	Mode 1	Mode 2	Mode 3
Blevins fundamental frequency Eqn. (*Equation 5.41*)	1.163E+07	-	-
Semi-analytical (Section 5.3)	1.158E+07	6.58E+07	1.36E+08
Modal analysis (*Equation 5.42*)	1.157E+07	7.25E+07	2.03E+08
1DOF equation (*Equation 5.43*)	1.160E+07	-	-

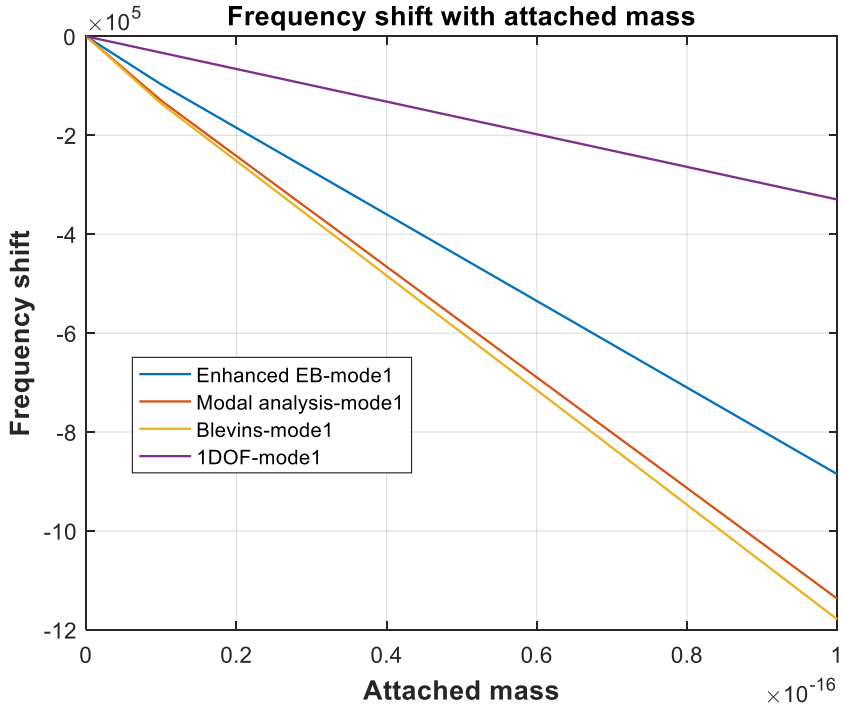

Figure 5.6 Comparison of frequency shift due to attached mass using 4 methods

Frequency shift of the NR due to a mass (3E-18 Kg) attached is compared for the 4 methods explained (Table 4: Resonance frequency of a beam with a mass of 3E-18 Kg attached at

the tip of the cantilever. Similarly, it is plotted for varying masses attached at the tip of the NR in the *Figure 5.6*.

This clearly shows that frequency shifts linearly with the attached mass. However, the shifts calculated using various methods are different and therefore, a method that is closely comparable to the Euler-Bernoulli equation (*Equation 5.38*) should be considered. This is very important for accurate mass measurements in mass sensing applications.

The 1DOF model, which is a well-established method, considers the mass to be uniformly distributed along the length of the NR. Consideration of location of the mass on the NR is important and is shown in the *Figure 5.5*. Blevins fundamental frequency equation shows a deviation of 1% from the E-B equation, when it is used to calculate the frequency of a beam without an attached mass. Enhanced E-B equation is more accurate than the modal analysis as shown in Table 1, when compared with the E-B equation. It quantifies the use of Enhanced E-B method over other methods.

5.5 Conclusion:

This chapter presents a derivation of a semi-analytical method to calculate frequencies of a nanobeam with varying Young's modulus (E) along its length. The results are compared against modal analysis and Euler-Bernoulli methods and the derived method is proved to be more accurate than the other methods described in the chapter and is very closely comparable to the Euler-Bernoulli equation for a beam of uniform *E*.

This derivation is further extended to calculate frequency of the nanocantilever with a mass attached at the tip of it. The frequency shifts due to different masses attached at the tip are calculated and compared against the other 4 methods described in the chapter. Using modal analysis, the resonance shift for masses attached at various points along the beam is presented. This shows that the assumption of a mass as uniformly distributed along the beam (based on 1DOF equation explained in the chapter) is a very rough approximation. The results for 4 different methods (Semi-analytical method, modal analysis, Blevins fundamental frequency equation and the 1DOF equation) are compared against the Euler-

Bernoulli method and the results for the Semi-analytical method are closest to those from the Euler-Bernoulli calculated values, for a beam of uniform stiffness and no attached mass.

Chapter 6: Conclusions and Future work

Nanocantilevers, with picogram level mass and resonance frequency in the MHz range, allow detection of added mass in the attogram range. Resonance frequency measurement is therefore an attractive method for molecular mass sensing. Ideally, for a given cantilever, the measured resonance frequency shift should depend solely on the attached mass without the influence of measurement method or other factors. Softening of the nanowire due to laser heating will lead to reduction in mass resolution and may also deform the nanowire. This thesis quantifies the frequency shift due to thermal laser-nanowire interaction.

In this thesis, the finite difference method is employed to calculate the temperature distribution of the nanowire, with convective and radiative boundary conditions. A semi-analytical method as an extension to Euler-Bernoulli framework for simple beam theory is derived to calculate the mass attached to a beam of varying stiffness.

The main conclusions of this thesis are:

1. For the NWs considered (made of Si, with length L = 6μm, diameter d = 400nm), the rate of thermal energy coupled into the NW (q) was varied and the temperature distribution calculated using a radiative boundary condition. The calculation predicts tip temperature would exceed the melting point for q = 2.6 mW.
2. The temperature distribution due to laser heating can cause a significant shift in the resonance frequency of NWs. As an example, for the NWs studied, results show that thermal energy rate, q = 2 mW can cause a relative frequency shift of 2400 ppm compared to 1-10 ppm or less due to minimum resolvable added mass. Small fluctuations in laser power could therefore create significant noise in frequency-based instruments.
3. Resonance amplitude calculations based on structural damping show that there can be about 77% reduction in amplitude between the least (0.1) and the highest (0.9) damping values. These values can help select the gap between the NR and the substrate, if the applied force is known.

4. This work includes the derivation of a Semi-analytical method, the only one known to the author that enables calculation of the resonance frequency of a cantilever beam of varying stiffness with a mass attached to its tip. Results obtained from this method for an unloaded, constant stiffness beam, are closely comparable to the value from the Euler-Bernoulli equation.
5. An effective Young's modulus value is calculated based on the derived Semi-analytical method, to obtain the frequency of the NW for a given laser power.
6. The capabilities listed in points 4 and 5 above could allow for correction to added mass calculated from measured resonant frequency.

Future work:

The investigations that would be useful to pursue in future are listed below:

1. Although the temperatures were calculated by assuming various values of coupled laser power, there is a need to measure and quantify the coupled laser power. A model to do so would likely use the wavelength of light and spot size of the laser, camera sensitivity, polarization of light, angle between incident light and the NW, optical properties of silicon etc. Knowledge of Maxwell's equations and Mie theory could be useful in calculating the thermal energy input to the NW.
2. Temperature distribution of the NW were calculated only for the case where the laser is focused on the end. Different points on the nanowire may be considered for the laser to be focused on and the variation in temperature profile should be studied.
3. Since the laser intensity presents a 'Gaussian power profile', the part of the NW intercepting the laser beam is to be considered for an accurate estimate of temperature profile. Experimental validation of frequency shift based on variation in laser power should be used to compare results that are calculated numerically.
4. Damping factor in this work was assumed in the range of 0.1 to 0.9 so as to be in the underdamped state. However, the exact value is unknown and could benefit from modeling of the internal dissipation regarded as phonon-phonon interactions.

Such models should include the time-dependent local stress field and thermoelastic damping.

5. For values of nanowire temperature far below the melting point, the temperature dependence of Young's modulus could be experimentally determined based on the measured frequency.

Bibliography

1. Thundat, T., Warmack, R. J., Chen, G. Y., & Allison, D. P. (1994). Thermal and ambient-induced deflections of scanning force microscope cantilevers. *Applied Physics Letters*, *64*(21), 2894-2896.
2. Dohn, S., Sandberg, R., Svendsen, W., & Boisen, A. (2005). Enhanced functionality of cantilever based mass sensors using higher modes. *Applied Physics Letters*, *86*(23), 233501.
3. Ekinci, K. L., Huang, X. M. H., & Roukes, M. L. (2004). Ultrasensitive nanoelectromechanical mass detection. *Applied Physics Letters*, *84*(22), 4469-4471.
4. Jensen, K., Kim, K., & Zettl, A. (2008). An atomic-resolution nanomechanical mass sensor. *Nature Nanotechnology*, *3*(9), 533.
5. Ono, T., Li, X., Miyashita, H., & Esashi, M. (2003). Mass sensing of adsorbed molecules in sub-picogram sample with ultrathin silicon resonator. *Review of Scientific Instruments*, *74*(3), 1240-1243.
6. Ekinci, K. L., Yang, Y. T., & Roukes, M. L. (2004). Ultimate limits to inertial mass sensing based upon nanoelectromechanical systems. *Journal of Applied Physics*, *95*(5), 2682-2689.
7. Mamin, H. J., & Rugar, D. (2001). Sub-attonewton force detection at millikelvin temperatures. *Applied Physics Letters*, *79*(20), 3358-3360.
8. Lavrik, N. V., Sepaniak, M. J., & Datskos, P. G. (2004). Cantilever transducers as a platform for chemical and biological sensors. *Review of Scientific Instruments*, *75*(7), 2229.
9. Eom, K., Park, H. S., Yoon, D. S., & Kwon, T. (2011). Nanomechanical resonators and their applications in biological/chemical detection: nanomechanics principles. *Physics Reports*, *503*(4-5), 115-163.
10. Ahumada, O., Pérez-Madrigal, M. D. M., Ramirez, J., Curcó, D., Esteves, C., Salvador-Matar, A., ... & Alemán, C. (2013). Sensitive thermal transitions of nanoscale polymer samples using the bimetallic effect: Application to ultra-thin polythiophene. *Review of Scientific Instruments*, *84*(5), 053904.

11. Soccio, M., Luongo, G., Esteves, C., Salvador-Matar, A., Ahumada, O., Rueda, D. R., ... & Ezquerra, T. A. (2014). Thermomechanical response of a semicrystalline polymer in the vicinity of the melting by using microcantilever technology. *Applied Physics Letters*, *104*(25), 251904.
12. Ekinci, K. L., & Roukes, M. L. (2005). Nanoelectromechanical systems. *Review of Scientific Instruments*, *76*(6), 061101.
13. Boukai, A. I., Bunimovich, Y., Tahir-Kheli, J., Yu, J. K., Goddard Iii, W. A., & Heath, J. R. (2011). Silicon nanowires as efficient thermoelectric materials. In *Materials for Sustainable Energy: A Collection of Peer-Reviewed Research and Review Articles from Nature Publishing Group* (pp. 116-119).
14. Fan, Z., Ho, J. C., Jacobson, Z. A., Yerushalmi, R., Alley, R. L., Razavi, H., & Javey, A. (2008). Wafer-scale assembly of highly ordered semiconductor nanowire arrays by contact printing. *Nano Letters*, *8*(1), 20-25.
15. Dasgupta, N. P., Sun, J., Liu, C., Brittman, S., Andrews, S. C., Lim, J., ... & Yang, P. (2014). 25th anniversary article: Semiconductor nanowires –synthesis, characterization, and applications. *Advanced Materials*, *26*(14), 2137-2184.
16. Sam, M., Moghimian, N., & Bhiladvala, R. B. (2016). Field-directed chaining of nanowires: towards transparent electrodes. *Materials Letters*, *163*, 205-208.
17. Ekinci, K. L. (2005). Electromechanical transducers at the nanoscale: actuation and sensing of motion in nanoelectromechanical systems (NEMS). *Small*, *1*(8-9), 786-797.
18. Sridaran, S., & Bhave, S. A. (2011). Electrostatic actuation of silicon optomechanical resonators. *Optics Express*, *19*(10), 9020-9026.
19. Rosa, M. A., De Bruyker, D., Völkel, A. R., Peeters, E., & Dunec, J. (2004). A novel external electrode configuration for the electrostatic actuation of MEMS based devices. *Journal of Micromechanics and Microengineering*, *14*(4), 446.
20. Nayfeh, A. H., & Younis, M. I. (2005). Dynamics of MEMS resonators under superharmonic and subharmonic excitations. *Journal of Micromechanics and Microengineering*, *15*(10), 1840.
21. Cheng, H. M., Ewe, M. T., Chiu, G. T., & Bashir, R. (2001). Modeling and control of piezoelectric cantilever beam micro-mirror and micro-laser arrays to reduce image

banding in electrophotographic processes. *Journal of Micromechanics and Microengineering*, *11*(5), 487.

22. Sam, M. (2016). *Controlling field-directed assembly of nanowires: towards nanomanufacturing for biosensors and transparent electrodes* (PhD dissertation), University of Victoria.
23. Weng, F. (2016). *Nanomechanical sensors: analyzing effects of laser-nanowire interaction and electrodeposited clamps on resonance spectra* (Master's thesis), University of Victoria.
24. Matsuura, T., Fukami, T., Chabloz, M., Sakai, Y., Izuo, S. I., Uemura, A., ... & Hamanaka, K. (2000). Silicon micro optical switching device with an electromagnetically operated cantilever. *Sensors and Actuators A: Physical*, *83*(1-3), 220-224.
25. Gil-Santos, E., Ramos, D., Pini, V., Llorens, J., Fernández-Regúlez, M., Calleja, M., ... & San Paulo, A. (2013). Optical back-action in silicon nanowire resonators: bolometric versus radiation pressure effects. *New Journal of Physics*, *15*(3), 035001.
26. Yu, M., Stott, S., Toner, M., Maheswaran, S., & Haber, D. A. (2011). Circulating tumor cells: approaches to isolation and characterization. *The Journal of cell Biology*, *192*(3), 373-382.
27. Sieuwerts, A. M., Kraan, J., Bolt, J., van der Spoel, P., Elstrodt, F., Schutte, M., ... & Foekens, J. A. (2009). Anti-epithelial cell adhesion molecule antibodies and the detection of circulating normal-like breast tumor cells. *Journal of the National Cancer Institute*, *101*(1), 61-66.
28. Sioss, J. A., Bhiladvala, R. B., Pan, W., Li, M., Patrick, S., Xin, P., ... & Clawson, G. A. (2012). Nanoresonator chip-based RNA sensor strategy for detection of circulating tumor cells: response using PCA3 as a prostate cancer marker. *Nanomedicine: Nanotechnology, Biology and Medicine*, *8*(6), 1017-1025.
29. Bhiladvala, R. B. (2012). Nanomechanical Resonant Sensors and Fluid Interactions. In *Encyclopedia of Nanotechnology* (pp. 1630-1643). Springer, Dordrecht.
30. Carr, D. W., Evoy, S., Sekaric, L., Craighead, H. G., & Parpia, J. M. (1999). Measurement of mechanical resonance and losses in nanometer scale silicon wires. *Applied Physics Letters*, *75*(7), 920-922.

31. O'Mahony, C., Hill, M., Hughes, P. J., & Lane, W. A. (2002). Titanium as a micromechanical material. *Journal of Micromechanics and Microengineering*, *12*(4), 438.
32. Fang, W., & Wickert, J. A. (1996). Determining mean and gradient residual stresses in thin films using micromachined cantilevers. *Journal of Micromechanics and Microengineering*, *6*(3), 301.
33. Wang, M. C., & Gates, B. D. (2009). Directed assembly of nanowires. *Materials Today*, *12*(5), 34-43.
34. Hanay, M. S., Kelber, S., Naik, A. K., Chi, D., Hentz, S., Bullard, E. C., ... & Roukes, M. L. (2012). Single-protein nanomechanical mass spectrometry in real time. *Nature Nanotechnology*, *7*(9), 602.
35. Syms, R. R. A. (2002). Long-travel electrothermally driven resonant cantilever microactuators. *Journal of Micromechanics and Microengineering*, *12*(3), 211.
36. Meyer, G., & Amer, N. M. (1988). Erratum: Novel optical approach to atomic force microscopy [Appl. Phys. Lett. 5 3, 1045 (1988)]. *Applied Physics Letters*, *53*(24), 2400-2402.
37. Favero, I., & Karrai, K. (2009). Optomechanics of deformable optical cavities. *Nature Photonics*, *3*(4), 201.
38. Belov, M., Quitoriano, N. J., Sharma, S., Hiebert, W. K., Kamins, T. I., & Evoy, S. (2008). Mechanical resonance of clamped silicon nanowires measured by optical interferometry. *Journal of Applied Physics*, *103*(7), 074304.
39. Fukuma, T., Kimura, M., Kobayashi, K., Matsushige, K., & Yamada, H. (2005). Development of low noise cantilever deflection sensor for multienvironment frequency-modulation atomic force microscopy. *Review of Scientific Instruments*, *76*(5), 053704.
40. Gysin, U., Rast, S., Ruff, P., Meyer, E., Lee, D. W., Vettiger, P., & Gerber, C. (2004). Temperature dependence of the force sensitivity of silicon cantilevers. *Physical Review B*, *69*(4), 045403.
41. Yang, C. K., Bossche, A., French, P. J., Gavan, K. B., van der Zant, H. S., Sadeghian, H., ... & van der Drift, E. W. (2009, October). Effect of laser deflection on resonant cantilever sensors. In *Sensors, 2009 IEEE* (pp. 869-872). IEEE.

42. Aguilar Sandoval, F., Geitner, M., Bertin, É., & Bellon, L. (2015). Resonance frequency shift of strongly heated micro-cantilevers. *Journal of Applied Physics*, *117*(23), 234503.
43. Sahai, T., Bhiladvala, R. B., & Zehnder, A. T. (2007). Thermomechanical transitions in doubly-clamped micro-oscillators. *International Journal of Non-Linear Mechanics*, *42*(4), 596-607.
44. Green, M. A. (2008). Self-consistent optical parameters of intrinsic silicon at 300 K including temperature coefficients. *Solar Energy Materials and Solar Cells*, *92*(11), 1305-1310.
45. Anaya, J., Torres, A., Martín-Martín, A., Souto, J., Jiménez, J., Rodríguez, A., & Rodríguez, T. (2013). Study of the temperature distribution in Si nanowires under microscopic laser beam excitation. *Applied Physics A*, *113*(1), 167-176.
46. Bronstrup, G., Jahr, N., Leiterer, C., Csáki, A., Fritzsche, W., & Christiansen, S. (2010). Optical properties of individual silicon nanowires for photonic devices. *ACS Nano*, *4*(12), 7113-7122.
47. Wang, J., Gudiksen, M. S., Duan, X., Cui, Y., & Lieber, C. M. (2001). Highly polarized photoluminescence and photodetection from single indium phosphide nanowires. *Science*, *293*(5534), 1455-1457.
48. Li, M., Bhiladvala, R. B., Morrow, T. J., Sioss, J. A., Lew, K. K., Redwing, J. M., ... & Mayer, T. S. (2008). Bottom-up assembly of large-area nanowire resonator arrays. *Nature Nanotechnology*, *3*(2), 88.
49. Gao, J., Yue, Y., Xie, D., & Xiong, Y. (2017). Thermal Characterization of Microscale Heat Convection under Rare Gas Condition by a Modified Hot Wire Method. *arXiv preprint arXiv:1709.02192*.
50. Darbandi, M., & Roohi, E. (2011). DSMC simulation of subsonic flow through nanochannels and micro/nano backward-facing steps. *International Communications in Heat and Mass Transfer*, *38*(10), 1443-1448.
51. Ho, C. M., & Tai, Y. C. (1998). Micro-electro-mechanical-systems (MEMS) and fluid flows. *Annual Review of Fluid Mechanics*, *30*(1), 579-612.
52. Tunc, G., & Bayazitoglu, Y. (2001). Heat transfer in microtubes with viscous dissipation. *International Journal of Heat and Mass Transfer*, *44*(13), 2395-2403.

53. Glassbrenner, C. J., & Slack, G. A. (1964). Thermal conductivity of silicon and germanium from 3 K to the melting point. *Physical Review*, *134*(4A), A1058.
54. Prakash, C. (1978). Thermal conductivity variation of silicon with temperature. *Microelectronics Reliability*, *18*(4), 333.
55. Pendry, J. B. (1999). Radiative exchange of heat between nanostructures. *Journal of Physics: Condensed Matter*, *11*(35), 6621.
56. Hopcroft, M. A., Agarwal, M., Park, K. K., Kim, B., Jha, C. M., Candler, R. N., ... & Kenny, T. W. (2006, January). Temperature compensation of a MEMS resonator using quality factor as a thermometer. In *Proc. 19th IEEE Int. Conf. MEMS* (pp. 222-225).
57. Ewins, D. J. (1984). *Modal testing: theory and practice* (Vol. 15). Letchworth: Research studies press.
58. Mohanty, P., Harrington, D. A., Ekinci, K. L., Yang, Y. T., Murphy, M. J., & Roukes, M. L. (2002). Intrinsic dissipation in high-frequency micromechanical resonators. *Physical Review B*, *66*(8), 085416.
59. Macioce, P. (2003). Viscoelastic damping 101. *Sound and Vibration Magazine*, *4*, 4-5.
60. Swarnakar, A. K., Van der Biest, O., & Vanhellemont, J. (2014). Determination of the Si Young's modulus between room and melt temperature using the impulse excitation technique. *Physica Status Solidi (c)*, *11*(1), 150-155.
61. Dunseith, D. P., Truppe, S., Hendricks, R. J., Sauer, B. E., Hinds, E. A., & Tarbutt, M. R. (2015). A high quality, efficiently coupled microwave cavity for trapping cold molecules. *Journal of Physics B: Atomic, Molecular and Optical Physics*, *48*(4), 045001.
62. Blevins, R. D. Formulas for natural frequency and mode shape, 1979. *Kreiger Publ. Comp., New York*.
63. Weaver Jr, W., Timoshenko, S. P., & Young, D. H. (1990). *Vibration problems in Engineering*. John Wiley & Sons.
64. Elishakoff, I., & Candan, S. (2001). Apparently first closed-form solution for vibrating: inhomogeneous beams. *International Journal of Solids and Structures*, *38*(19), 3411-3441.

65. Huang, Y., & Li, X. F. (2010). A new approach for free vibration of axially functionally graded beams with non-uniform cross-section. *Journal of Sound and Vibration*, *329*(11), 2291-2303.
66. Ece, M. C., Aydogdu, M., & Taskin, V. (2007). Vibration of a variable cross-Section beam. *Mechanics Research Communications*, *34*(1), 78-84.
67. Kwak, D., Kim, J., Park, S., Ko, H., & Cho, D. I. (2003, January). Why is (111) silicon a better mechanical material for MEMS: torsion case. In *ASME 2003 International Mechanical Engineering Congress and Exposition* (pp. 259-264). American Society of Mechanical Engineers.
68. Moran, M. J., Shapiro, H. N., Munson, B. R., & DeWitt, D. P. (2003). Introduction to thermal systems engineering. *Thermodynamics, Fluid Mechanics, and Heat Transfer, John Wiley & Sons*.

Appendix A:

1. MATLAB code for temperature profile of NW considering conduction and/or convection

```
clear;
close all;
format long
n = 100;                %no. of sections , where no. of nodes is n+1
L =6*(10^-6);           %length of NW in m
r= 2*(10^-7);           %radius of NW in m
h=25;                   %convective co-eff W/m2K
k=148;                  %thermal conductivity of silver W/mK
p=2*pi*r;               %perimeter in m
Ac=pi*(r^2);            %cross-sectional area in m2
Ts=298;                 %surrounding temp in kelvin
Tb=299;                 %Base temp in kelvin
deltax = L/n;
deltaksi=1/n;           %Non-dimensional length ksi=x/L
Bi=h*L/ k;              %Biot number (dimensionless)
P=0.005;                %Heat input in W
F=0.4;                  %Fraction of laser power being absorbed
q=-P*F;                 %Heat transfer rate W
alpha=-(q*L)/(k*Ac*(Tb-Ts));    %dy/dksi at tip which = conduction heat transfer rate
beta=-6*deltaksi*alpha;         %denominator of dy/dksi taken to Rhs
m=sqrt((h*p)/(k*Ac));           %fin parameter
for i=1:n+1
   ksi(i,1)=deltaksi*(i-1);     %Non-dimensional length ksi=x/L
   gamma(i,1)=(-Bi*p*L)/Ac;     %co-efficient y(i)
end
for i=1:n
   a(i,1)=-2+ (gamma(i)*(deltaksi^2)); %c(i)y(i-1) + a(i)y(i) + b(i)y(i+1)
   b(i,1)=1;
   c(i,1)=1;
   d(i,1)=0;
end
a(n+1)=18;
b(n+1)=-11;
c(n+1)=-9;
d(n+1)=beta;
%% Neumann BC tip condition after eliminating y(n-2) & y(n-1)
star1 = a(n+1) - 2 - a(n)*c(n+1) + 2*a(n)*a(n-1);
star2 = b(n+1) - b(n)*c(n+1) + 2*b(n)*a(n-1);
%% creating the problem matrices %l-c,di-a,u-b;rhs-v
```

```
l(1,1) = 0; l(n+1,1) = star1;
u(1,1) = 0; u(n+1,1) = 0;
di(1,1) = 1; di(n+1,1) = star2;
v(1,1) = 1;
v(n+1,1) = d(n+1);

for i=2:n
l(i,1) =  c(i);
u(i,1) = b(i);
di(i,1) = a(i);
v(i,1) = 0;
end

%% thomas algorithm
for i = 1:n
   % normalize by dividing with d(i)
   u(i) = u(i)/di(i);
   v(i) = v(i)/di(i);
   di(i) = 1;
   % using pivot element for elimination
   smt = l(i+1);    l(i+1) = 0;    di(i+1) = di(i+1) - smt*u(i);
   v(i+1) = v(i+1) - smt*v(i);
end
%% back-substitution
y = zeros(n+1,1);
y(n+1,1) = v(n+1)/di(n+1);
for i = n:-1:1
   y(i) = v(i) - u(i)*y(i+1);
end
T = zeros(n+1,1);
for i=1:n+1
    x(i,1)=deltax*(i-1);
   T(i)=((Tb-Ts)*y(i))+Ts;
   theta(i,1)=T(i,1)-Ts;
   thetab=Tb-Ts;
   y(i)=theta(i)/thetab;
end
  M=(sqrt(h*p*k*Ac)) * thetab;
%% proof sinh
 ym=zeros(n+1,1);
 for i=1:n+1
 ym(i,1)=(((theta(n+1)/thetab)*sinh(m*x(i)))+sinh(m*(L-x(i))))/sinh(m*L);
end
%ym
%% Dirichlet BC for comparison of data
alpha1= (h*p*(deltax^2))/(k*Ac);%co-efficient during discretization
```

```
beta1 = -alpha1*Ts;            %co-eff in discretization
e=2.71;                %logarithmic e
%% creating the problem matrices
ln(1,1) = 0; ln(n+1,1) = 0;
un(1,1) = 0; un(n+1,1) = 0;
din(1,1) = 1; din(n+1,1) = 1;
vn(1,1) = 299; %technically tells T1=600
vn(n+1,1) = T(n+1) ;%310; %technically Tn+1=298

ln(2:n,1) =  1;
un(2:n,1) = 1;
din(2:n,1) = -(2+alpha1);
vn(2:n,1) = beta1;
%% thomas algorithm
for i = 1:n
   % normalize by dividing with d(i)
   un(i) = un(i)/din(i);
   vn(i) = vn(i)/din(i);    din(i) = 1;
   % using pivot element for elimination
   smtn = ln(i+1);    ln(i+1) = 0;    din(i+1) = din(i+1) - smtn*un(i);
   vn(i+1) = vn(i+1) - smtn*vn(i);
end
%% back-substitution
Tn = zeros(n+1,1);Tn(n+1) = vn(n+1)/din(n+1);
for i = n:-1:1
   Tn(i) = vn(i) - un(i)*Tn(i+1);
end
y1n=zeros(n+1,1);
y1n(n+1,1)=0;
 for i=1:n+1
 thetan(i,1)=Tn(i,1)-Ts;
 thetab=Tb-Ts;
 y1n(i)=thetan(i)/thetab;
 end
 %% non-dimensional nodes
 deltaksi=1/n;
for i=1:n+1
ksi(i,1)=deltaksi*(i-1);
end

 %% proof sinh
 ym1=zeros(n+1,1);
 for i=1:n+1
 ym1(i,1)=(((theta(n+1)/thetab)*sinh(m*x(i)))+sinh(m*(L-x(i))))/sinh(m*L);
 end
Incr = 11;
```

```
Indices = 1:Incr:length(ksi);
PointPlot=plot(ksi(Indices), y(Indices), 'R-',ksi(Indices), ym(Indices),
'bo','LineWidth',1.1);
legend(PointPlot, 'y (CFD code-Neumann)', 'ym (Euler-Bernoulli solution-Neumann)');
hold on
Incrn = 7;
Indicesn = 1:Incrn:length(ksi);
Incrn1 = 17;
Indicesn1 = 1:Incrn1:length(ksi);
PointPlot=plot(ksi(Indicesn), y1n(Indicesn), 'ks',ksi(Indicesn1), ym1(Indicesn1),
'g*','LineWidth',1.1);
legend(PointPlot, 'y1n (CFD code-dirichlet)', 'ym1 (Euler-Bernoulli solution-dirichlet)');
legend('Location','southeast');
title('Temperature at \xi=0 and flux at \xi=1','FontSize',12,'FontWeight','bold')
xlabel('Non-dimensional length of the NW, \xi=x/L','FontSize',12,'FontWeight','bold')
ylabel('Non-dimensional Temperature, y = \theta /
\thetab','FontSize',12,'FontWeight','bold')
grid on
```

Appendix B:

Analytical equation used to validate the convection process

Analytical equation used[68]:

$$\frac{\theta}{\theta_b} = \frac{\left(\theta_L / \theta_b\right) \sinh mx + \sinh m(L - x)}{\sinh mL}$$

where $\theta = T - T_s$, $\theta_b = T_b - T_s$ and $\theta_L = \theta(L)$.

The non-dimensional temperature, 'Y' is given by:

$$Y = \frac{\theta}{\theta_b} = \frac{T - T_s}{T_b - T_s}$$

Appendix C:

MATLAB code for temperature profile of NW considering Radiation

```
clear;
close all;
format long
n = 1000;                %no. of sections , where no. of nodes is n+1
L =6*(10^-6);            %length of NW in m
r= 2*(10^-7);            %radius of NW in m
p=2*pi*r;                %perimeter in m
Ac=pi*(r^2);             %cross-sectional area in m2
As=p*L;                  %Surface area
Ts=298;                  %surrounding temp in kelvin
Tb=299;                  %Base temp in kelvin
deltax = L/n;
deltaksi=1/n;            %Non-dimensional length ksi=x/L
P=0.004;                 %Heat input in W
F=0.4;                   %Fraction of laser power being absorbed
q=-P*F;                  %Heat transfer rate W
sigma=5.67*(10^-8);    % stefan-boltzmann constant
e=0.6;                   %epsilon
tol= 1.0e-08;            %tolerance error
for i=1:n+1
   x(i,1)=deltax*(i-1);
   ksi(i,1)=deltaksi*(i-1);
end

   %% ****************Assumption temperatures (T(i,1) & y(i,1))***********
   for i=1:n+1
      T(i,1) = 0.98*(x(i)^6) + 2*(x(i)^5) + 12*(x(i)^4) + 36*(x(i)^3) + 92*(x(i)^2) +
1.5e+02*(x(i)) + 1;
   end
   %% iteration starts!
iter=5000;
for j=1:iter
   for i=1:n+1
      theta(i,1)=T(i,1)-Ts;
      thetab=Tb-Ts;
      y(i,1)=theta(i,1)/thetab;
      %% addition of T dependant k of silicon
```

```
      k(i,1)=115598*(T(i)^-1.177);%thermal conductivity of silicon W/mK
     dkdt(i,1)=-1.36058846e+05* (T(i)^-2.177);
     alpha(i)=-(q*L)/(k(i)*Ac*(Tb-Ts)); %gradiant dy/dksi(instead of dt/dx) at tip
which=conduction heat transfer rate (Neumann BC)
      beta(i)=6*deltaksi*alpha(i);      %denominator of dy/dksi taken to Rhs
   end
   %% Code with only radiation
   %% defining co-effs [gamma(ksi), H(ksi)]
   for i=1:n+1
      gamma(i,1)=(-(e*sigma*(L^2)*(Ts^3)*p)/(k(i)*Ac))*((T(i)/Ts)^3 + (T(i)/Ts)^2
+(T(i)/Ts) + 1);%y*gamma(ksi)
   end
   H(1,1)=(dkdt(i)/k(i))*L*(T(2)-T(1))/(deltax);      %dy/dksi *(h(ksi))
   H(n+1,1)=(dkdt(i)/k(i))*L*(T(n+1)-T(n))/(deltax);
   for i=2:n
      H(i,1)=(dkdt(i)/k(i))*L*(T(i+1)-T(i-1))/(2*deltax);
   end
   %% defining co-effs b,a,c - from taylor's series %ci*y(i-1) +  ai*y(i) + bi*y(i+1)
   for i=1:n
      a(i,1)=-2+((deltaksi^2)*gamma(i));
      b(i,1)=1+((deltaksi/2)*H(i));
      c(i,1)=1-((deltaksi/2)*H(i));
      d(i,1)=0;
   end
   a(n+1)=18;
   b(n+1)=-11;
   c(n+1)=-9;
   d(n+1)=-beta(i);
  %% Neumann BC tip condition after eliminating y(n-2) & y(n-1) terms
   star1 = a(n+1)*c(n-1) - 2*b(n-1) - a(n)*c(n+1)*c(n-1) + 2*a(n)*a(n-1);
   star2 = b(n+1)*c(n-1) - b(n)*c(n+1)*c(n-1) + 2*b(n)*a(n-1);
%% creating the problem matrices
   %sub-diaganol, diagonal, super-diaganol represented by l,di,u,v
   l(1,1) = 0; l(n+1,1) = star1;
   u(1,1) = 0; u(n+1,1) = 0;
   di(1,1) = 1; di(n+1,1)=star2;
   v(1,1) = 1;
   v(n+1,1) = d(n+1)*c(n-1);

   l(2:n,1) = c(i);
   u(2:n,1) = b(i);
   di(2:n,1) = a(i);
   v(2:n,1) = 0;
   %% thomas algorithm, smt - Forward elimination starts
   for i = 1:n
      % normalize by dividing with dn(i)
```

```
        u(i) = u(i)/di(i);
        v(i) = v(i)/di(i);
        di(i) = 1;
        % using pivot element for elimination
        smt = l(i+1);    l(i+1) = 0;    di(i+1) = di(i+1) - smt*u(i);
        v(i+1) = v(i+1) - smt*v(i);
    end
    %% back-substitution to get non-dimensional temperature y(i,2)
    y(n+1,2) = v(n+1)/di(n+1);
    for i = n:-1:1
        y(i,2) = v(i) - u(i)*y(i+1,2);
    end
    %% dimensional temperature in a loop for convergence T(i,2)
    for i=1:n+1
        T(i,2)= (y(i,2)*(Tb-Ts))+Ts;
    end
    %% convergence criteria % relative convergence test
    SumErr=0;
    for i=2:n+1

      Err(i,1)=(abs( (T(i,2)-T(i,1)) / T(i,2) ) );
      SumErr= SumErr + Err(i);
    end
    AvgErr=SumErr/n;
    maxErr=max(Err);
        if maxErr > tol
            T(:,1)=T(:,2);
            y(:,1)=y(:,2);
        else
            L2=2;
            break
        end
end
T(n+1,1)
%% comparison with analytical solution
const=e*sigma*(Ts^3);
h1(i,1)=const*((T(i,1)/Ts)^3 + (T(i,1)/Ts)^2 +(T(i,1)/Ts) + 1);
Incr = 10;
Indices = 1:Incr:length(ksi);
PointPlot=plot(ksi(Indices), y(Indices));%, 'b-', 'R-',ksi(Indices), ym(Indices), 'bo');
legend(PointPlot, 'y (Neumann CFD code)');%, 'ym (Analytical solution)');
legend('Location','southeast');
grid on
title('Neumann radiation for 3mW of laser power and 40% being absorbed by SiNW')
%title
xlabel('Non-dimensional length of the NW, \xi= x/L') % x-axis label
```

```
ylabel('Non-dimensional Temperature, y = \theta / \thetab') % y-axis label
```

Appendix D:

MATLAB code for frequency response functions

```
clear;
close all;
hold on
format long
n=100;                  %no. of elements
N=n+1;                  %no. of nodes
dof=2*N;                %degrees of freedom
L=6*(10^-6);            %length of NW in m
r=2*(10^-7);            %radius of NW in m
Ac=pi*(r^2);            %cross-sectional area in m2
deltax = L/n;
rho=2330;               %material density in [kg/m^3] of Si
for i=1:n+1
   x(i,1)= deltax*(i-1);
end
% min=0.2*2*0.01;
% max=.3*2*0.01;
% eta_r=min+rand(n,1)*(max-min);
% eta = sort(eta_r,'descend');
eta=0.2*2*0.01; %Loss factor %
% E_r=-7.8e9*(ksi.^4) + 6.1e9*(ksi.^3) - 5.3e9*(ksi.^2) - 1.2e9*ksi + 1.3e11; %in Pa

% for j=1:n
% E(j,1)=(1+1i*eta(j))*E_r(j);
% % E(j,1)=(1+1i*eta)*E_r(j);
% end
% E=127.33975e9*(1+1i*eta) ;        %Young's modulus in [Pa] of Si
E=123.33975e9*(1+1i*eta) ;
I= pi*(r^4)/4;
%% stiffness matrix

KG=[6 3*deltax -6 3*deltax;
   3*deltax 2*(deltax^2) -3*deltax deltax^2;
   -6 -3*deltax 6 -3*deltax;
   3*deltax deltax^2 -3*deltax 2*(deltax^2)];

Ke=zeros(4,4*n);
for i=1:1:n
   Ke(:,4*i-3:4*i)= ((2*E* I)/(deltax^3))* KG;
%     Ke(:,4*i-3:4*i)= ((2*E(i)* I)/(deltax^3)) * KG;
end
K = zeros(2*N,2*N);
```

```
for i=1:n
   K(2*i-1:2*i+2,2*i-1:2*i+2)=K(2*i-1:2*i+2,2*i-1:2*i+2)+Ke(:,4*i-3:4*i);
end
%% Consistent mass-matrix

MG=[156 22*deltax 54 -13*deltax;
   22*deltax 4*(deltax^2) 13*deltax -3*(deltax^2);
   54 13*deltax 156 -22*deltax;
   -13*deltax -3*(deltax^2) -22*deltax 4*(deltax^2)];

Me = (rho*Ac*deltax/420) * MG;

M = zeros(2*N,2*N);
for i=1:2:(2*N)-3
   M(i:(3+i),i:(3+i))= M(i:(3+i),i:(3+i)) + Me;
end
%% Calculation of Damping Matrix
% C=zeta*2*sqrt(K*M);
%% Boundary Conditions
K=K(3:2*N,3:2*N);
M=M(3:2*N,3:2*N);
% C=C(3:2*N,3:2*N);
%% Solving Eigen Problem
% [v,d] = eig(K,M);    % v-eigenvectors;d-eigenvalues
[v,d] = eig(M\K);
omegar=sqrt(d);         %in rad/sec
f=omegar/(2*pi);        %Get frequencies in hertz or cycles/sec
f(1)
%% Modal mass and stiffness
mr=v'*M*v;              % Reduced mass
kr=v'*K*v;              % stiffness matrix
% cr=v'*C*v;            % Damping matrix
phi=zeros(2*n,2*n);
for i=1:(2*n)
   for j=1:(2*n)
      phi(i,j)= v(i,j)/sqrt(mr(j,j));    % mass-normalised eigenvectors for mode shape
   end
end

%% FRF

Counter=1;
f1=9e6:1e3:13e6;
omega=f1*2*pi;

for i_omega=1:length(omega)
```

```
    a=0;
    for i=1:2*n
        a=a+((phi(2*n-1,i)^2)/(omegar(i,i)^2 - omega(i_omega)^2 + 1i*0*(omegar(i,i)^2)
));
    end
    alpha(Counter)=a;
    Counter=Counter+1;
end
plot(omega/2/pi,abs(alpha))
grid on
hold on
title('Frequency response analysis for stiff or soft cantilever','FontSize',12) %title
xlabel('frequency (Hz)','FontSize',12,'FontWeight','bold') % x-axis label
ylabel('Amplitude (m)','FontSize',12,'FontWeight','bold') % y-axis label
```

Appendix E:

MATLAB code for Semi-analytical method to calculate frequency of a beam with varying *E* and an attached mass

```
clear
close all
format long
n=10;
L=6*(10^-6);            %length of NW in m
r=2*(10^-7);            %radius of NW in m
I= pi*(r^4)/4;
E0=1.3e+11;
Ac=pi*(r^2);            %cross-sectional area in m2
rho=2330;               %density in kg/m3
mass=rho*Ac;            %mass in kg
N=n+1;
deltaksi=1/n;
ksi=zeros(N,1);
s=zeros(N,1);
emn=zeros(N,N);
K1mn=zeros(N,N);
K2mn=zeros(N,N);
K3m=zeros(N,N);
%% emn

for m=1:N
   for n=1:N
      syms ksi
       E= E0;
       %E=E0*(- 0.06125*ksi.^4 + 0.0479*ksi.^3 - 0.04162*ksi.^2 - 0.009423*ksi +
1.02089);
       D=E*I;
       emn(m,n)=int((ksi.^(m+n))*D,ksi,0,1);
   end
end

%% K1mn

for m=1:N
   for n=1:N
       syms s ksi
       E= E0;
       %E=E0*(- 0.06125*s.^4 + 0.0479*s.^3 - 0.04162*s.^2 - 0.009423*s + 1.02089);
```

```
      D=E*I;
      K1=(diff(diff(D,s),s)*(ksi-s))-(2*(diff(D,s)));
      K1mn(m,n)=double(int(int(K1*(ksi^m)*(s^n),s,0,ksi),ksi,0,1));
   end
end
%% K2mn

for m=1:N
   for n=1:N
      syms s ksi
      E= E0;
%       E=E0*(- 0.06125*s.^4 + 0.0479*s.^3 - 0.04162*s.^2 - 0.009423*s + 1.02089);
      D=E*I;
      A11=int(s^2*(s-(3*ksi))*s.^n,s,0,ksi);
      A12=int(ksi^2*(ksi-(3*s))*s.^n,s,ksi,1);
      A1=A11+A12;
      K2=((mass*ksi.^m)/6)*A1;
      K2mn(m,n)=int(K2,ksi,0,1);
   end
end
%% K3m

for m=1:N
   for n=1:N
     syms ksi
      E= E0;
      %E=E0*(- 0.06125*ksi.^4 + 0.0479*ksi.^3 - 0.04162*ksi.^2 - 0.009423*ksi +
1.02089);
      D=E*I;
      K3m(m,n)=int(((-3*ksi.^2) + (ksi.^3))*(ksi.^(m+n)),ksi,0,1);
   end
end

%% solve 'k'
m0=1e-16;          % attached mass
cf=(m0/6/L);       %coefficien]]AAAA=(K2mn+(cf*K3m));
syms k
solk=det(emn + K1mn + (k*(K2mn+(cf*K3m))))==0;
solk1=det(emn + K1mn + (k*(K2mn)))==0; % no mass attached
k=double(abs((solve(solk,k))));
k = sort(k,'ascend');
k(3)=[];

%% natural frequencies
```

```
f1=[11581390.0057507;65780498.8759194;136191297.469645;143140178.788834;1556
34402.724176;179398494.042475;225404455.728853;324034104.537805;584096627.65
0773;1651895268.86361];
omega=sqrt(k/L^4);                    % k = omega^2 * L^4
f=double(omega/2/pi);
```

Appendix G:

MATLAB code for analytical equation to calculate frequency of a beam with uniform *E*

```
clear
close all;
format long
L=6*(10^-6);          %length of SiNW in m
R=2*(10^-7);          %radius of SiNW in m
D=2*R;
A=pi*(R^2);           %cross-sectional area in m2
Ix= pi*(R^4)/4;
E=1.3e+11;
rho=2330;             %material density in [kg/m^3] of Si


mb=rho*A*L;           % mass of beam
modes=10;             %number of modes and mode shapes to be computed:
   Nm=3*modes;
   jj=1;
  while jj<=Nm
          betaNL(jj)=fzero(@(betaNL)cosh(betaNL)*cos(betaNL)+1,[jj jj+3]);
       jj=jj+3;
  end

   index=(betaNL~=0);
   betaN=(betaNL(index))';
   for k=1:length(betaN)
      wn(k,1)=((betaN(k)^2)*D*sqrt(E))/(4*(L^2)*sqrt(rho));  %angular frequency (rad/s)
      fn(k,1)=wn(k,1)/(2*pi);
   end
```